The Astrophysical Journal, 849:157 (18pp), 2017 November 10 https://doi.org/10.3847/1538-4357/aa937f

Multiwavelength Stellar Polarimetry of the Filamentary Cloud IC5146. I. Dust Properties

Jia-Wei Wang[1], Shih-Ping Lai[2], Chakali Eswaraiah[2,3,4], Dan P. Clemens[5], Wen-Ping Chen[3], and Anil K. Pandey[4]
[1] Institute of Astronomy, National Tsing Hua University, 101, Section 2, Kuang-Fu Road, Hsinchu 30013, Taiwan, R.O.C; jwwang@gapp.nthu.edu.tw
[2] Institute of Astronomy & Department of Physics, National Tsing Hua University, 101, Section 2, Kuang-Fu Road, Hsinchu 30013, Taiwan, R.O.C; slai@phys.nthu.edu.tw
[3] Institute of Astronomy, National Central University, 300 Jhongda Road, Taoyuan 32001, Taiwan, R.O.C; eswarbramha@gmail.com, wchen@gm.astro.ncu.edu.tw
[4] Aryabhatta Research Institute of Observational Sciences (ARIES), Manora-peak, Nainital, Uttarakhand-state, 263002, India; pandey@aries.res.in
[5] Institute for Astrophysical Research, Boston University, 725 Commonwealth Avenue, Boston, MA 02215, USA; clemens@bu.edu

Received 2017 August 9; revised 2017 September 22; accepted 2017 October 5; published 2017 November 10

Abstract

We present optical and near-infrared stellar polarization observations toward the dark filamentary clouds associated with IC5146. The data allow us to investigate the dust properties (this paper) and the magnetic field structure (Paper II). A total of 2022 background stars were detected in the R_c, i', H, and/or K bands to $A_V \lesssim 25$ mag. The ratio of the polarization percentage at different wavelengths provides an estimate of $\lambda_{\max}$, the wavelength of the peak polarization, which is an indicator of the small-size cutoff of the grain size distribution. The grain size distribution seems to significantly change at $A_V \sim 3$ mag, where both the average and dispersion of P_{R_c}/P_H decrease. In addition, we found $\lambda_{\max} \sim 0.6$–$0.9\ \mu$m for $A_V > 2.5$ mag, which is larger than the $\sim 0.55\ \mu$m in the general interstellar medium (ISM), suggesting that grain growth has already started in low-A_V regions. Our data also reveal that polarization efficiency ($\mathrm{PE} \equiv P_\lambda/A_V$) decreases with A_V as a power law in the R_c, i', and K bands with indices of -0.71 ± 0.10, -1.23 ± 0.10, and -0.53 ± 0.09. However, H-band data show a power index change; the PE varies with A_V steeply (index of -0.95 ± 0.30) when $A_V < 2.88 \pm 0.67$ mag, but softly (index of -0.25 ± 0.06) for greater A_V values. The soft decay of PE in high-A_V regions is consistent with the radiative alignment torque model, suggesting that our data trace the magnetic field to $A_V \sim 20$ mag. Furthermore, the breakpoint found in the H band is similar to that for A_V, where we found the P_{R_c}/P_H dispersion significantly decreased. Therefore, the flat PE–A_V in high-A_V regions implies that the power-index changes result from additional grain growth.

Key words: dust, extinction – ISM: clouds – ISM: individual objects (IC5146) – ISM: magnetic fields – ISM: structure – polarization

Supporting material: machine-readable table

1. Introduction

The linearly polarized background starlight observed in early studies (Hall 1949; Hiltner 1949a) was suggested to result from dichroic absorption by nonspherical dust grains aligned to B fields (Hiltner 1949b). Hence, polarized starlight is commonly used as a tracer of the B-field structure in the plane of sky (e.g., Chapman et al. 2011; Clemens et al. 2012c; Eswaraiah et al. 2012). The first theory to explain dust alignment used a paramagnetic mechanism (DG alignment; Davis & Greenstein 1951). However, later studies revealed timescale and efficiency problems, so other alignment mechanisms were offered, including superparamagnetic grains (Jones & Spitzer 1967) and superthermal rotation rates (Purcell 1979). Nevethless, most of these mechanisms are only efficient for particular physical conditions, and fail to explain the polarization observed across a wide variety of environments (see review in Andersson et al. 2015).

The model of radiative alignment torques (RATs; Dolginov & Mitrofanov 1976; Draine & Weingartner 1996, 1997; Lazarian & Hoang 2007) can currently best explain how dust grains align with B fields. The RATs theory assumes an anisotropic radiation field impacting nonspherical dust grains. The radiation field can generate net torque on the grains and induce both spin of the grains and precession about the B field. For typical interstellar radiation fields, the RATs alignment timescale is much faster than DG alignment (Lazarian & Hoang 2007), and superthermal rotation tends to enhance RATs alignment more than DG alignment (Hoang & Lazarian 2009). In addition, RATs is efficient across a variety of environments, and thus more likely dominates the grain alignment process.

A key prediction of the RATs theory is the decreasing polarization efficiency (PE, P_λ/A_V) with increasing A_V, because the radiation field required to align the dust grains is decreased through extinction (Lazarian et al. 1997). In order to examine whether the RATs theory can explain observed polarizations, Whittet et al. (2008) performed a numerical simulation based on RATs theory and assuming a starless core with only an external radiation field and a fixed dust grain size distribution for all A_V. Their simulation results matched their K-band polarimetry data toward Taurus up to at least $A_V \sim 10$ mag; the K-band polarization degree varied with A_V as a power law, with $P_\lambda/\tau_K \propto A_V^{-0.52}$. In addition, their simulation predicted that the RATs mechanism would cease as A_V approached 10 mag, since the radiation that can penetrate to such high column densities has wavelengths too long to effectively align the grains. However, the single power-law matched their data over the $A_V = 0$–30 mag range well, which was inconsistent with the predicted cessation of alignment at $A_V \sim 10$ mag. To explain the inconsistency, Whittet et al. (2008) argued that the RAT mechanism may still work in high-A_V regions if (1) the dust grains have undergone significant growth and so can couple to longer wavelength radiation, or (2) embedded stars are present to provide radiation at shorter wavelength to enhance the alignment of small dust grains.

To further test the RATs theory in dense clouds, Jones et al. (2015) used both infrared and submillimeter polarimetry data to trace the variation of polarization efficiency (PE) up to $A_V \sim 100$ mag within starless cores. They found a change of power-law index for PE versus extinction from -0.5 to -1 at $A_V \sim 20$ mag, consistent with the cessation of alignment predicted by Whittet et al. (2008). In addition, Jones et al. (2016) found a deeper break point at $A_V \sim$ hundreds mag and a reversed trend such that the power-law index of PE versus A_V changed from -1 to -0.5 within the Class 0 YSO G034.43 +00.24 MM1. The opposite trends shown in these two cases suggest that dust alignment in dense clouds could be strongly affected by environmental effects.

In the RATs paradigm, the polarization degree is expected to be wavelength dependent because the cloud extinction penetration is wavelength dependent and because the highest alignment efficiency occurs at wavelengths similar to the sizes of the grains (Cho & Lazarian 2005; Lazarian & Hoang 2007). Therefore, the polarization wavelength-dependence is determined by both the extinction and the size of dust grains, resulting in a polarization spectrum exhibiting a single peak ($\lambda_{\max}$). Kim & Martin (1995) showed that $\lambda_{\max}$ is sensitive to the small-size cutoff of the grain size distribution, since the dust size distribution is a power law and the small-size cutoff will effectively determine the mean size of the dust grains. Whittet et al. (2008) calculated the $\lambda_{\max}$ variation with A_V using a RATs model with a fixed grain size distribution over A_V, and showed that the RATs theory can explain their observed dependence of $\lambda_{\max}$ increasing with A_V to ~6 mag, but that RATs predicts that $\lambda_{\max}$ flattens for higher A_V in the Taurus cloud.

Recent observational results are mostly consistent with the RATs theory (Whittet et al. 2008; Alves et al. 2014; Cashman & Clemens 2014), although the dust alignment efficiency varies from source to source. As an extreme case, Goodman et al. (1995) found a constant near-infrared polarization degree toward L1755 for A_V of 1–10 mag, and argued that near-infrared polarization can only trace the B field on the surfaces of dark clouds. In contrast, other observations mostly showed a polarization degree increasing with A_V, such as $P \propto A_V^{0.48}$ toward Taurus (Whittet et al. 2008) and $P \propto A_V^{0.26}$ toward the L204 cloud 3 (Cashman & Clemens 2014), suggesting that the constant polarization degree found in Goodman et al. (1995) represented a special case and was not the norm.

It is still unclear why the P–A_V relation found in L1755 is different from the relation found for other clouds. Whittet et al. (2008) reanalyzed the L1755 polarimetry data with a better background star selection and extinction estimation, but still found the same relation. They speculated that this unique relation might result from a lack of the typical physical conditions leading to grain alignment inside this cloud or a reduction of observed polarization that is due to the complex B-field structure within the L1755 filaments. To examine these possibilities, more polarimetry observations covering both a wider area and more wavebands could help to reveal the alignment conditions for dust grains with different sizes and to probe the detailed B-field structure. In addition, since the Goodman et al. (1995) polarization detections only spanned a small range of A_V (2–8 mag), it would be of interest to perform polarization observations with higher sensitivity to investigate this relation to higher A_V values.

An ideal target for a detailed testing of the RATs paradigm is the system of dark cloud filaments associated with the reflection and emission nebula IC5146, a nearby (~460 pc) star-forming region in Cygnus. The system consists of a young cluster inside an H II region and a long main dark cloud filament with several subfilaments branching out from the main filament. The *Herschel* Gould Belt Survey (Arzoumanian et al. 2011) revealed a complex network of filaments within the long dark cloud, highlighting the locations of young forming stars. The *Planck* polarization map of IC5146 (Planck Collaboration et al. 2016c) revealed that the B field is nearly uniform, with the millimeter-wavelength-traced B field oriented perpendicular to the elongation orientation of the main filament. This apparently uniform B field gives the IC5146 dark cloud system an advantage for testing the RATs model because the high angular resolution of stellar polarizations can be used to test for, and quantify, complex B fields along the multiple line of sights.

In a series of papers, we will report measurements and analyses of the polarizations of stars behind the IC5146 filamentary cloud. The polarimetry of background starlight was performed at both optical and infrared wavelengths to probe the large-scale B field in the cloud. In this paper, we focus on the dust properties and the dust alignment conditions revealed by our data in order to identify where the B fields were accurately probed by our observations. The observations and data reduction are described in Section 2. In Section 3 we present the polarization measurements toward IC5146. Section 4 presents an initial analysis of the data to show how the dust grain alignment conditions vary with A_V and regions. In Section 5 we discuss the evolution of dust grains and how the dust properties influence the PE. The consequences of these results for the investigations of the role of B fields in cloud evolution will be offered in the forthcoming Paper II.

2. Observations and Data Reduction

We measured the polarization of background stars toward the IC5146 filamentary cloud system with several instruments: the Aryabhatta Research Institute of Observational Sciences (ARIES) Imaging Polarimeter (AIMPOL; Rautela et al. 2004) and Triple-Range (g', r', i') Imager and POLarimeter (TRIPOL; S. Sato et al. 2017, in preparation) provided optical R_c- and i'-band polarimetry data, respectively. Mimir (Clemens et al. 2007) measured the H- and K-band polarizations at near-infrared wavelengths. Figure 1 shows the target fields for each instrument overlaid on the *Herschel* archive 250 μm image (Griffin et al. 2010; Arzoumanian et al. 2011). The dust continuum map shows an east-west main filament connected to the bright cluster complex, known as the Cocoon Nebula. Numerous "subfilaments" are extended from the main filament, with the largest subfilament located on the northwest side of the main filament. Almost all parts of the cloud were observed with Mimir, while the fields observed with AIMPOL were chosen to be mainly in the edge of the cloud in order to cover as many optically bright stars as possible. The TRIPOL observations focused on the northwestern region, with longer exposure time, where bright stars are rare at both optical and infrared wavelengths. The detailed information of the observations with the different instruments is described below.

2.1. AIMPOL Polarimetry

The R_c-band (0.67 μm, bandwidth = 0.14 μm) polarimetric observations were carried out toward the IC5146 filamentary

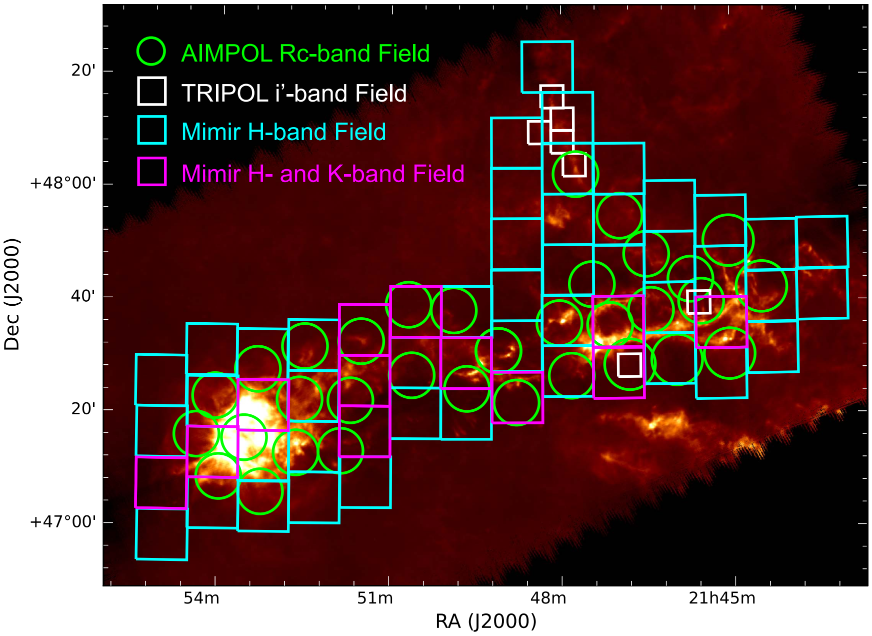

Figure 1. IC5146 fields surveyed in our polarization observations overlaid on the *Herschel* 250 μm image. The fields observed with TRIPOL and AIMPOL are labeled with white boxes and green circles, respectively. The magenta boxes show the fields observed with Mimir using the H and K bands, and the cyan boxes show the fields observed with Mimir using only the H band.

cloud system using AIMPOL, which is mounted at the Cassegrain focus of the 104 cm Sampurnanand telescope of the ARIES, Nainital, India. AIMPOL consisted of a half-wave plate (HWP) modulator and a Wollaston prism beam-splitter illuminating a fraction (370 × 370 pixel^2) of the Tektronics 1024 × 1024 pixel^2 CCD camera. The pixel size of the CCD was 1.73″ and the typical seeing was ∼2″. The observations spanned the nights of 2011 November 4–8 and 2012 November 8–15 and covered 37 fields (see Figure 1), with each field having a useful diameter of ∼8′. In order to obtain Stokes Q and U, we took images at four independent HWP orientations (0°, 22°.5, 45°, and 67°.5; Schaefer et al. 2007). The Wollaston prism analyzer produced offset, but simultaneous, ordinary and extraordinary overlapping images for each HWP orientation. Hence, each image resulted in one measurement of Stokes Q or U. The integration time was set to 10 minutes for each HWP orientation, so the total integration time for each field was 40 minutes.

The polarization measurements were calibrated for instrumental polarization and offset angle by observing standard polarized and unpolarized stars drawn from Schmidt et al. (1992). The data were reduced using standard IRAF procedures.[6] The fluxes in the ordinary and extraordinary beams for each observed source were extracted using standard aperture photometry. Sources with stellar overlap, fewer than 10% of the total sources, were excluded. The polarization degree and angle for each star were derived from the relative fluxes in the ordinary and extraordinary beams. We removed the Ricean bias with the asymptotic estimator

$$P = \sqrt{(U^2 + Q^2) - \sigma_P^2}, \qquad (1)$$

where P is the debiased degree of polarization, Q and U are normalized Stokes Q and U, and σ_P is the uncertainty in the polarization percentage (Wardle & Kronberg 1974). The details of the observing facility and procedures used to estimate the polarization degree and polarization angles (P.A.) are described in Eswaraiah et al. (2011, 2012).

2.2. TRIPOL Polarimetry

Polarimetric observations focused on the northwestern region of IC5146 in the i' bands (0.77 μm, bandwidth 0.15 μm) on 2012 July 27–28 and 2014 July 6 with TRIPOL installed on the Lulin-One-meter Telescope in Lulin Observatory, Taiwan. Seven fields, each with a size of 4′ × 4′, were observed (see Figure 1). TRIPOL consisted of dichroic mirrors and three ST-9 512 × 512 pixel^2 CCD cameras, which enabled simultaneous observations in the g', r', and i' bands; however, only the i'-band data were able to detect background stars behind this dark cloud. The pixel sizes of the CCDs were 0.5 arcsec and the average seeing was ∼1.″5. A rotatable achromatic half-wave plate and a fixed wire-grid were used to analyze the incoming light. Each field was measured at four HWP orientations (0°, 22°.5, 45°, and 67°.5, with pairs of images yielding stellar Stokes Q and U values.). The integration time for each position angle was 22.5 minutes, so each field required a total of 1.5 hours.

Standard reduction procedures were applied using IRAF, and the photometry of each background star was obtained using Source Extractor (Bertin & Arnouts 1996). The debiased polarization degree and angle for each background star were derived from the fluxes measured through each of the four HWP orientation angles and calibrated against observations of polarized and unpolarized standard stars from Schmidt et al. (1992).

2.3. Mimir Polarimetry

We carried out H- (1.6 μm) and K-band (2.2 μm) polarization observations toward IC5146 on 2013 September 17–27,

---

[6] IRAF is distributed by the National Optical Astronomy Observatory, which is operated by the Association of Universities for Research in Astronomy (AURA) under a cooperative agreement with the National Science Foundation.

using the Mimir instrument (Clemens et al. 2007), which is mounted on the 1.8 m Perkins telescope located near Flagstaff, AZ, and operated by Lowell Observatory. Fifty-seven fields covering the IC5146 cloud were observed in the *H* band, and 12 fields were observed in the *K* band toward the dense regions (see Figure 1). The pixel size of the InSb detector array was 0.58 arcsec and the average seeing was $\sim 1\overset{\prime\prime}{.}5$. The field of view was $10' \times 10'$ for Mimir, and we set $1'$ overlap between adjacent fields. Each field was observed in six sky-dither positions where images were taken at 16 orientation angles of the HWP. A total of 96 (16 × 6) images were taken for each field with 10 sec of integration time for each image for both the *H* and *K* bands, and thus the total integration time was 16 minutes for each field. We took an additional short integration for fields with bright stars, which took 4 minutes per field.

In order to calibrate the nonlinearities of the InSb detector array, a series of images were taken with an increasing exposure time toward an illuminated flat-field screen, and the response curve of each pixel was fitted with a polynomial model to obtain a linearity correction. Flat fields for each HWP position were taken using a lights-on/lights-off method toward a flat-field screen inside the closed dome during the observation run. The data were calibrated using the Mimir Software Package Basic Data Processing (MSP-BDP), and the Photo POLarimetry tool (MSP-PPOL) was used to extract Stokes *Q* and *U* values for each observed source from the calibrated data. The detailed processes used in the Mimir Software Package are described in Clemens et al. (2012a, 2012b, 2012c).

3. Results

3.1. The Polarization Catalog

We matched the polarization data to the 2MASS catalog (Skrutskie et al. 2006) to obtain positions accurate to 0.5 arcsec. Table 1 lists all the observed polarization properties as well as photometric magnitudes from 2MASS and *WISE* (Wright et al. 2010). Column 1 lists the star number, and columns 2 and 3 list the R.A. and decl. The measured Stokes *Q*, *U*, debiased *P*, and position angle P.A. in the R_c, i', *H*, and *K* bands with their uncertainties are listed in columns 4–35. The *J*-, *H*-, *K*-, *W1*-, and *W2*-band magnitudes and uncertainties are listed in columns 36–45. Column 46 presents the estimated visual extinction described in Section 4.1. Column 47 present the Usage Flag (UF; stars with UF = 1 were selected for further analyses, and stars with UF = 0 were not used). The usage data were selected with the polarization degree divided by its uncertainty $P/\sigma_p \geqslant 3$ for the R_c and i' bands, and $P/\sigma_p \geqslant 2$ and $\sigma_p < 5\%$ for the *H* and *K* bands; the selection criteria were relaxed for near-infrared data, since the number of 3σ near-infrared detections was too small for adequate statistics.

In total, 2022 independent background stars have polarization detections in at least one of the four bands, 239 stars were detected in two bands, 24 stars were detected in three bands, and only 3 stars were detected in all four bands. About 71% of the background stars were detected in the *H* band, 24% in the R_c band, 10% in the i' band, and 8% in the *K* band.

Figure 2 shows all of the polarization measurements on the *Herschel* SPIRE 250 μm image. The inferred B field is seemingly perpendicular to the main filament on large scales but parallel to the subfilaments. The bimodal perpendicular or parallel alignment is similar to that seen in previous polarimetry work toward filamentary clouds, and has been ascribed to B-field confinement of sub-Alfvénic turbulence or gravitational contraction channeled by strong B fields (Li et al. 2013). We will discuss the B-field structure in detail and estimate the B-field strengths with the Chandrasehkar-Fermi method to determine the dynamical importance of the B fields in Paper II.

3.2. Consistency in P.A. between Multiple Wavelengths

To test whether the results from AIMPOL, TRIPOL, and Mimir were consistent and thereby capable of revealing wavelength-dependent effects in the probed dust columns, we selected the stars that had detections at multiple wavelengths, and we examine their P.A.s in the different wavelengths in Figure 3. In total, 143, 31, and 65 stars were selected in R_c–i', R_c–*H*, and *H*–*K* band pairs. The mean P.A. differences in these three band pairs were $-4\overset{\circ}{.}6 \pm 0\overset{\circ}{.}8$, $6\overset{\circ}{.}2 \pm 0\overset{\circ}{.}8$, and $-2\overset{\circ}{.}9 \pm 1\overset{\circ}{.}6$, respectively. The standard deviation of the measured P.A. differences were $8\overset{\circ}{.}7$, $16\overset{\circ}{.}3$, and $26\overset{\circ}{.}6$ for the R_c–i', R_c–*H*, and *H*–*K* band pairwise samples. The average expected uncertainties of P.A. difference, propagated from observational uncertainties $(\sigma_{P.A._{\lambda_1-\lambda_2}} = \sqrt{\sigma^2_{P.A._{\lambda_1}} + \sigma^2_{P.A._{\lambda_2}}})$, were $4\overset{\circ}{.}2$, $9\overset{\circ}{.}3$, and $12\overset{\circ}{.}3$ for the R_c–i', R_c–*H*, and *H*–*K* band pairwise samples. The P.A. difference standard deviations obtained from these sets are 1–2 times to the propagated instrumental uncertainties, which are acceptable values since the P.A.s may be intrinsically different at different wavelengths because they may trace the polarizations to different depths.

3.3. Negligible Foreground Contamination

We attempted to identify and exclude foreground stars whose polarizations do not trace the B field of the IC5146 cloud system. To obtain enough star samples to represent the foreground polarization near IC5146, we selected stars with known distances and *V*-band polarization measurements from van Leeuwen (2007) and Heiles (2000), within a 10° radius sky area near IC5146. Figure 4 shows the *V*-band polarization degree (P_V) versus distance for these 41 stars. The distance of 460^{+40}_{-60} pc to the IC5146 cloud system (Lada et al. 1999) was used to separate these stars into foreground and background groups. The polarization degree rises significantly at a distance of ∼400 pc, which is possibly due to nearby clouds in the Gould Belt. For most of the stars with distances smaller than 400 pc, the polarization degrees are below 0.3%. This value was chosen as the upper limit of the foreground *V*-band polarization for the sky area near IC5146.

In the interstellar medium (ISM), the polarization in the *V* band is greater than that in the R_c, *H*, or *K* bands (Serkowski 1973). Hence, based on the foreground star values in Figure 4, the foreground polarization in the R_c, *H*, and *K* bands is expected to be lower than ∼0.3%. This foreground polarization upper limit is similar to the instrumental uncertainties of our data (∼0.2%–0.5%). Hence, any foreground stars were likely to have been already excluded by our selection criteria ($P/\sigma_p > 3$ for the R_c and i' bands and $P/\sigma_p > 2$ for the *H* and *K* bands). Thus, we concluded that contamination by foreground stars was negligible in our sample set, and furthermore, that no foreground polarization correction to the remaining data was necessary.

Table 1
Measured Polarization Properties of Stars Probing the IC5146 Dark Cloud Complex

			R_c-band Polarimetry								i'-band Polarimetry				
ID (1)	R.A. (deg) (2)	Decl. (deg) (3)	Q_{R_c} (%) (4)	σ_{QR_c} (%) (5)	U_{R_c} (%) (6)	σ_{UR_c} (%) (7)	P_{R_c} (%) (8)	σ_{PR_c} (%) (9)	PA_{R_c} (deg) (10)	σ_{PAR_c} (deg) (11)	$Q_{i'}$ (%) (12)	$\sigma_{Q_{i'}}$ (%) (13)	$U_{i'}$ (%) (14)	$\sigma_{U_{i'}}$ (%) (15)	$P_{i'}$ (%) (16)
8327	326.3935	47.6311	1.68	0.32	1.94	0.33	2.54	0.34	24.51	3.44	1.59	0.07	2.18	0.07	2.70
12997	326.6920	47.4848	0.98	0.24	0.90	0.24	1.31	0.25	21.34	4.86	0.54	0.05	1.40	0.05	1.50
13793	326.7371	47.4965	2.11	0.18	1.40	0.18	2.53	0.18	16.75	1.97	2.16	0.05	1.75	0.05	2.78

			H-band Polarimetry								K-band Polarimetry						
$\sigma_{i'}$ (%) (17)	$PA_{i'}$ (deg) (18)	$\sigma_{PA_{i'}}$ (deg) (19)	Q_H (%) (20)	σ_{QH} (%) (21)	U_H (%) (22)	σ_{UH} (%) (23)	P_H (%) (24)	σ_H (%) (25)	PA_H (deg) (26)	σ_{PAH} (deg) (27)	Q_K (%) (28)	σ_{QK} (%) (29)	U_K (%) (30)	σ_{UK} (%) (31)	P_K (%) (32)	σ_{PK} (%) (33)	PA_K (deg) (34)
0.07	26.90	0.70	0.41	0.11	0.65	0.11	0.76	0.11	28.62	4.28	0.03	0.22	0.53	0.20	0.49	0.20	43.34
0.05	34.46	0.97	0.47	0.23	0.47	0.22	0.62	0.23	22.28	10.49	0.31	0.25	0.44	0.16	0.51	0.20	27.36
0.05	19.55	0.50	0.98	0.21	0.70	0.23	1.19	0.22	17.82	5.33	0.37	0.24	0.36	0.13	0.48	0.19	21.98

	2MASS Catalog						*WISE* Catalog					
σ_{PAK} (deg) (35)	J (mag) (36)	σ_J (mag) (37)	H (mag) (38)	σ_H (mag) (39)	K (mag) (40)	σ_K (mag) (41)	$W1$ (mag) (42)	σ_{W1} (mag) (43)	$W2$ (mag) (44)	σ_{W2} (mag) (45)	A_V[a] (mag) (46)	UF (47)
11.76	10.861	0.019	9.727	0.028	9.352	0.017	9.163	0.023	9.314	0.019	5.00	1
11.20	11.483	0.025	10.745	0.03	10.462	0.023	10.257	0.022	10.35	0.021	3.03	1
11.66	11.205	0.023	10.333	0.028	10.075	0.022	9.894	0.022	9.961	0.021	3.16	1

Note.
[a] The uncertainties of A_V are 0.93 mag, estimated in Section 3.1.

(This table is available in its entirety in machine-readable form.)

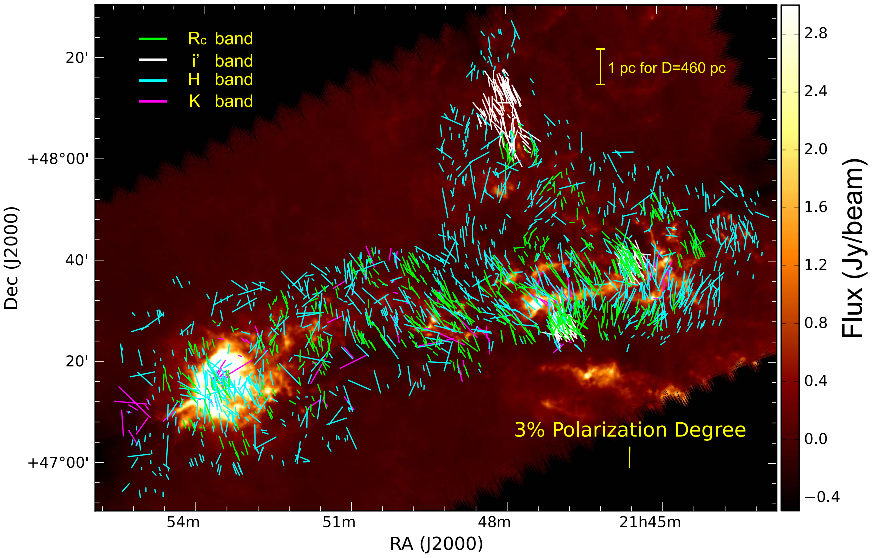

Figure 2. Map of IC5146 stellar polarizations overlaid on the *Herschel* 250 μm image, with an FWHM beamsize of 17$''$.6. The detections in the TRIPOL i' band, AIMPOL R_c band, and Mimir H and K band are labeled in white, green, cyan, and magenta.

4. Analysis

4.1. NICER Extinction

Visual extinction provides an estimate of how many dust grains are responsible for the observed starlight polarization, and thus is required for estimating dust alignment efficiency and testing the RATs theory. We used the technique called near-infrared color excess revisited (NICER; Lombardi & Alves 2001)[7] to calculate the visual extinction over the IC5146 cloud system. The NICER technique uses multiband colors to obtain extinction for a target field, using extinction coefficients derived from Indebetouw et al. (2005). We selected a total of

---

[7] Using the PNICER python package developed by Meingast et al. (2017).

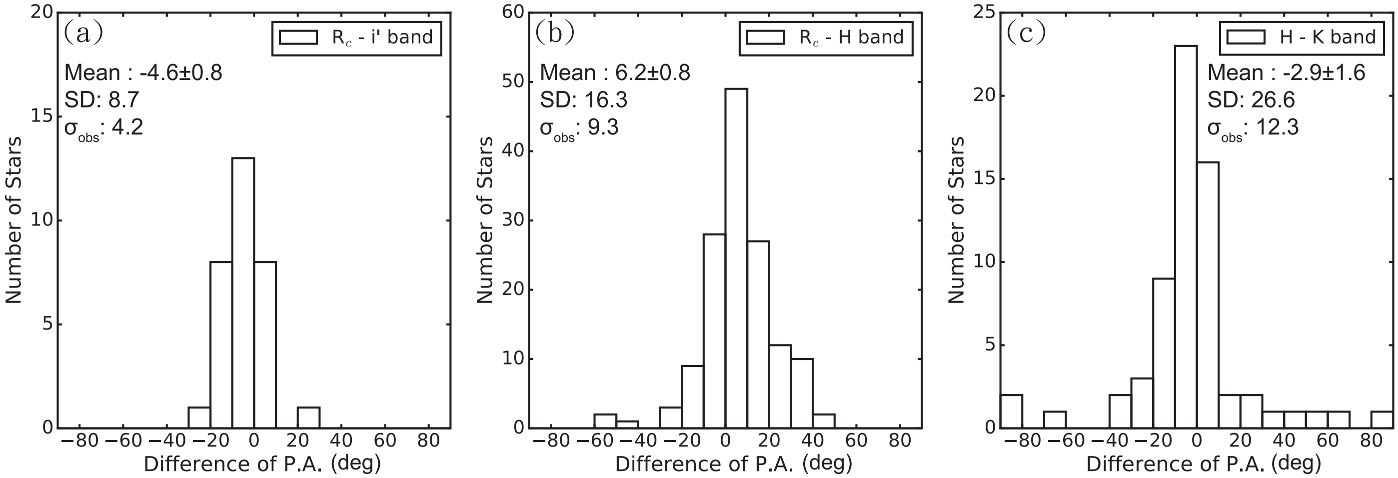

Figure 3. Examination of the P.A. consistency of the data for stars with polarization detections in multiple bands. The differences of P.A.s detected in different band pairs are shown in the histograms with the mean, standard deviation, and averaged instrumental uncertainty ($\sigma_{\rm obs}$) of the P.A.s for each band pair, listed in degrees. The comparisons between the R_c- and i'-band number of stars, R- and H-band number of stars, and H- and K-band number of stars are shown in panels (a), (b), and (c), respectively. Although small offsets and larger dispersions are shown in these band pairs compared to the instrumental uncertainties, about 90% of the stars are distributed within $3\sigma_{\rm ins}$.

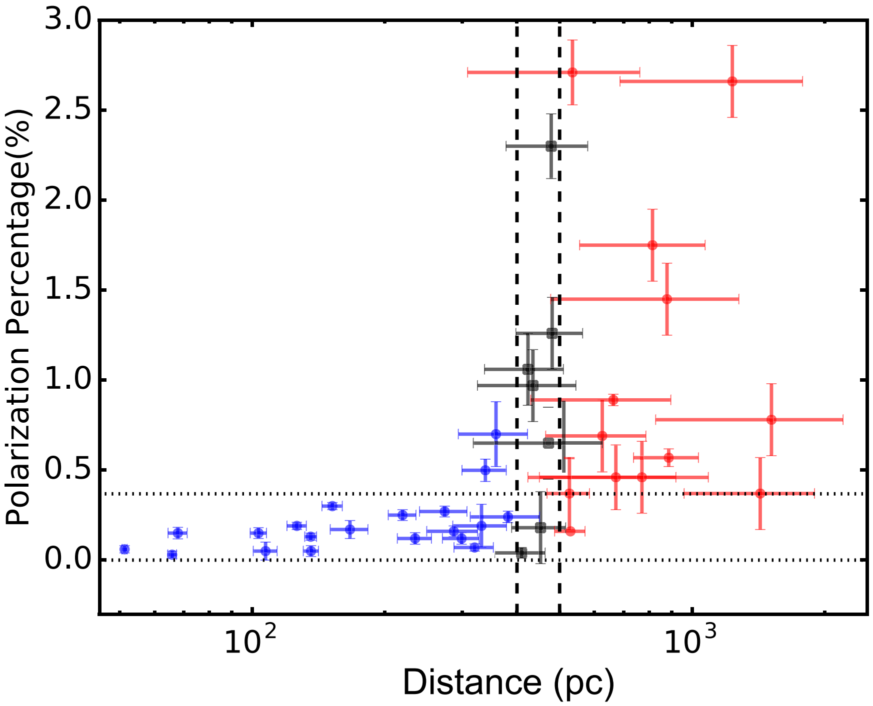

Figure 4. Polarization degree vs. distance for stars within 10° of IC5146 with distance measurements in the *Hipparcos* catalog (van Leeuwen 2007) and polarization measurements in Heiles (2000). The black vertical dashed lines represent the 1σ upper and lower boundary of the distance of the IC5146 dark cloud estimated by Lada et al. (1999). The blue, black, and red dots identify the stars as classfied by distance zone. The blue dot stars were used to estimate the foreground polarization to the IC5146 cloud system. The horizontal dotted lines show the estimated foreground polarization of 0%–0.3%.

186,319 stars from the 2MASS catalog and 46,100 stars from the *WISE* catalog that cover the IC5146 cloud system. To estimate the stellar intrinsic colors, a square control field, centered at R.A. = 330°.153, decl. = +47°.794 with a side length of 15′, was compared to the target field.

To examine the quality of the estimated extinctions, the NICER extinction map shown in Figure 5 was created and compared with the *Herschel* map. The extinction map was created from the variance-weighted mean of NICER extinction of each individual star within a pixel grid with a pixel size of 30″. The pixel grid was smoothed using a Gaussian weighting kernel with an FWHM of 90″. The black contours in Figure 5 show the *Herschel* 250 μm data. The morphology of the extinction map is almost identical to that of the 250 μm map.

Figure 6 shows the histogram of A_V values derived from the NICER analysis. The uncertainties in A_V arise both from the uncertainties of the spectral types and from the propagated photometric uncertainties. In order to estimate the overall uncertainty of A_V, we selected all the stars that NICER assigned with negative A_V, and assumed that the negative A_V values were only due to A_V uncertainties. This negative A_V portion of the full distribution was duplicated and reflected about $A_V = 0$ to generate a new pseudo-A_V distribution. Fitting this with a Gaussian centered at $A_V = 0$, we derived a standard deviation

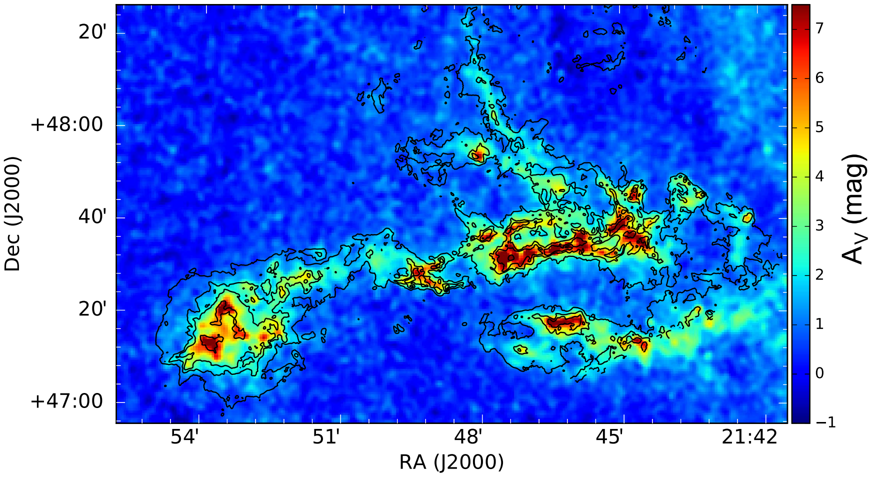

Figure 5. NICER extinction map across the IC5146 dark cloud. Visual extinction, in magnitudes of A_V, is displayed in color, and the black contour lines represent *Herschel* 250 μm intensities with levels of 0.1, 0.5, and 1.5 mJy/beam. The FWHM of the Gaussian smoothing kernel used to create the extinction map was 90″, and the FWHM beam size of *Herschel* 250 μm image is 18.″1. The extinction morphology and 250 μm intensity distribution are in close agreement.

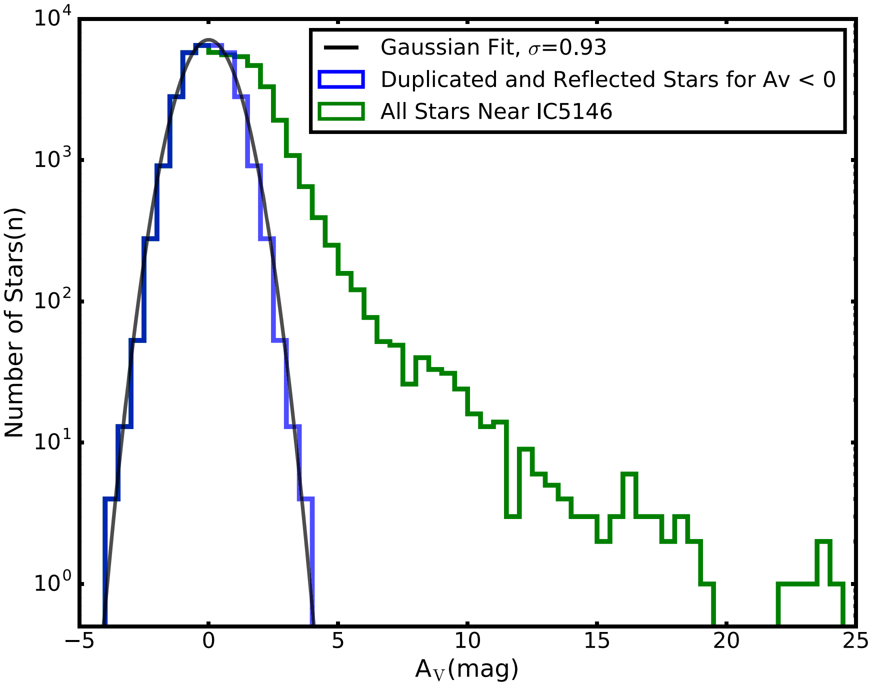

Figure 6. Histogram of A_V for the stars near IC5146 from the NICER analysis. In order to estimate the A_V uncertainty, the negative portion of the A_V distribution was duplicated and reflected about $A_V = 0$ to generate the pseudo-distribution shown in green. The best-fitting Gaussian, plotted in black, indicates a 1σ uncertainty of 0.93 mag.

of 0.93 mag. Because this includes uncertainties from both spectral typing and observations, we adopted this value as our A_V uncertainty.

4.2. Polarization Efficiency

To test whether the polarization measurements trace the magnetic field structure inside the IC5146 cloud system, we examined whether embedded dust grains align with the B fields via estimating how the degree of polarization varied with extinction. PE is defined as polarization percentage divided by A_V. It describes how much polarization is contributed by dust grains in the line of sight. We used PE versus A_V to test whether the dust grains are better aligned in the diffuse region, as predicted by the RATs model.

Figure 7 shows PE versus A_V for the R_c-band data. The data probability density over the PE–A_V space, represented by the contours, was calculated using the kernel density estimation (Rosenblatt 1956; Parzen 1962); for each source, the probability distribution function was described by a Gaussian kernel, and the width of the Gaussian kernel was determined by the uncertainties of PE and A_V. The probability density for the entire data set was represented by the summation of the Gaussian kernels.

To reduce the uncertainty from A_V and also avoid the bias due to uneven sampling over A_V, the variance-weighted means of PE and A_V were calculated in bins of width $\log(A_V) = 0.1$. The uncertainties of the weighted mean of PE and A_V for each bin were propagated from the instrumental uncertainty and A_V uncertainty for each sample. Stars that

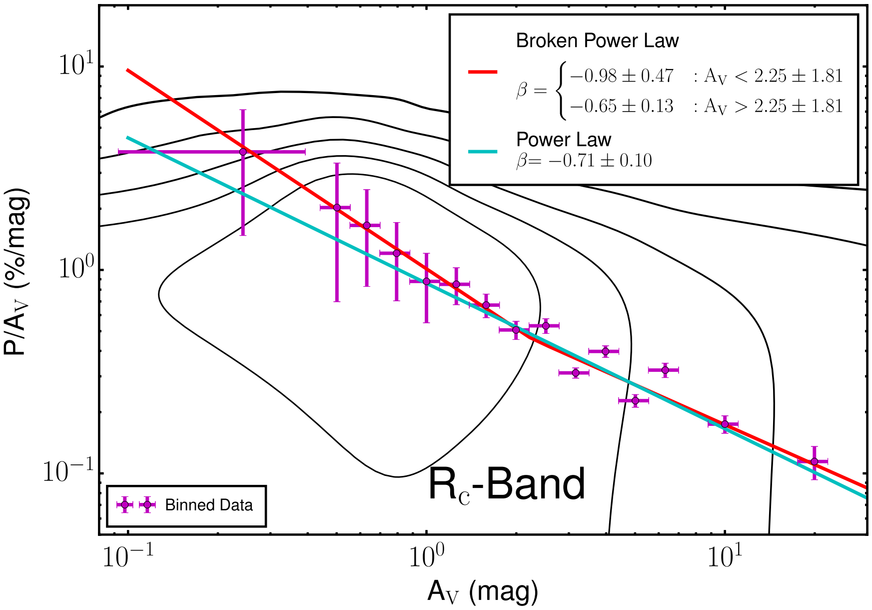

Figure 7. Polarization efficiency (PE) vs. A_V for R_c-band data. Black contours are drawn at 1%, 10%, 30%, 50%, and 70% of the peak data density. The purple points show the weighted mean PE in bins of width log $(A_V) = 0.1$. The uncertainties of PE for each bin are propagated from instrumental uncertainties, and the uncertainties of A_V are propagated from 0.93 mag for each source. Bins with $A_V < 0.5$ mag were merged to further reduce the uncertainties. The red and cyan lines plots the best-fit single power-law and broken power-law models to the binned data, respectively.

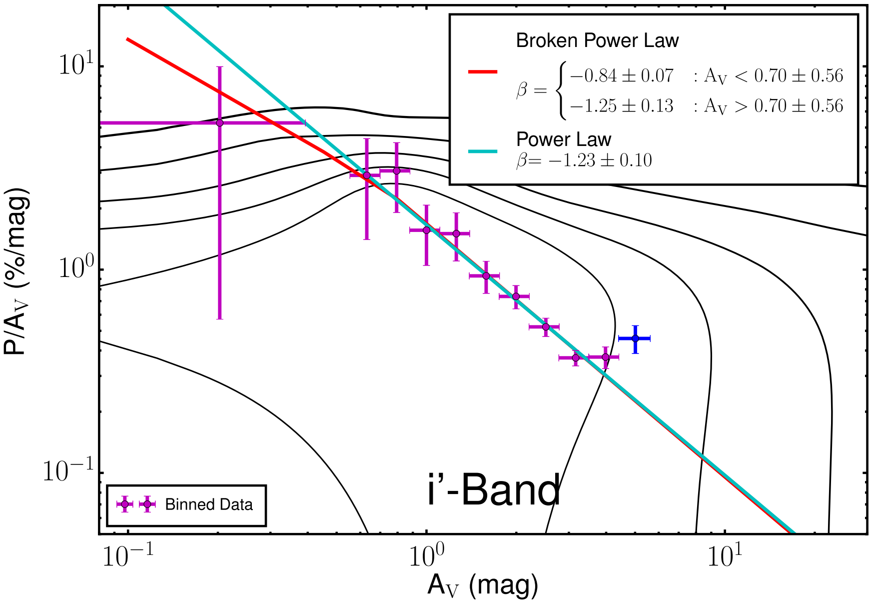

Figure 8. Same as Figure 7, but for i'-band data. The bin with the highest A_V, plotted in blue, contains only two stars that seem to have uncommonly high PE, and thus the bin was excluded from fitting.

NICER assigned with negative A_V were not used for PE determination, since their extinctions were negligible.

Similarly, PE versus A_V plots for the i', H, and K bands are shown in Figures 8, 9, and 10, respectively. In the i' band, the last bin ($A_V = 5$ mag) was found to have significantly higher PE and the bin only contained two stars. This bin was judged to be an outlier, and was excluded from further analysis. In the four bands, PE always decreased with A_V, but with different slopes. In addition, the PE at $A_V \sim 20$ mag is still half of the PE at $A_V \sim 4$ mag, suggesting that the dust grains in high-A_V regions are still being aligned with some degree of efficiency.

The power-law behavior of PE–A_V has been shown in previous studies (e.g., Whittet et al. 2008; Chapman et al. 2011; Cashman & Clemens 2014) and apears to match the prediction of the RATs theory well. However, recent studies have also discovered changes in the index of the power law for high-extinction regions (Alves et al. 2014; Andersson et al. 2015). To test whether in the IC5146 dark cloud system the power-law index changes with A_V, we fit P_λ/A_V versus A_V with both a single power law (hereafter, Model 1),

$$P_\lambda/A_V = \alpha A_V^{\beta}, \quad (2)$$

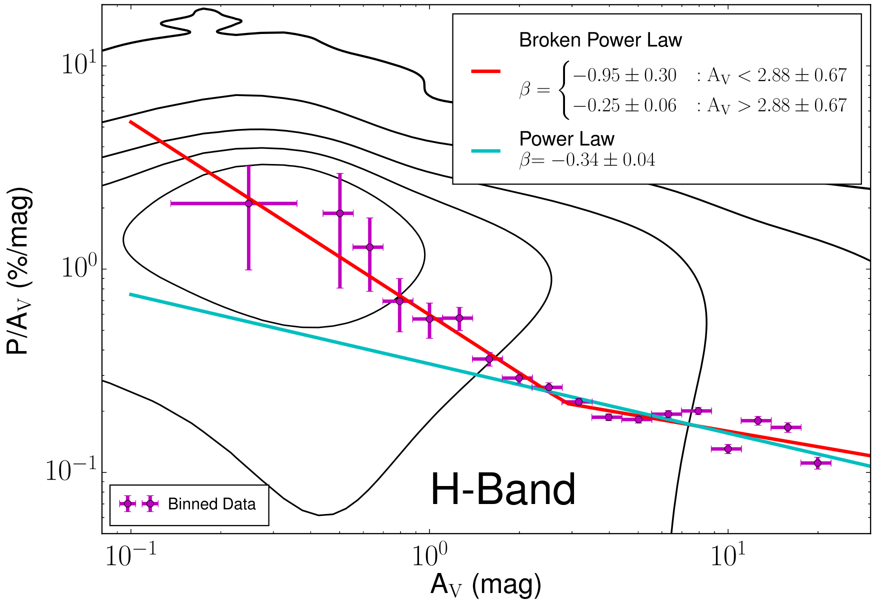

Figure 9. Same as Figure 7, but for *H*-band data.

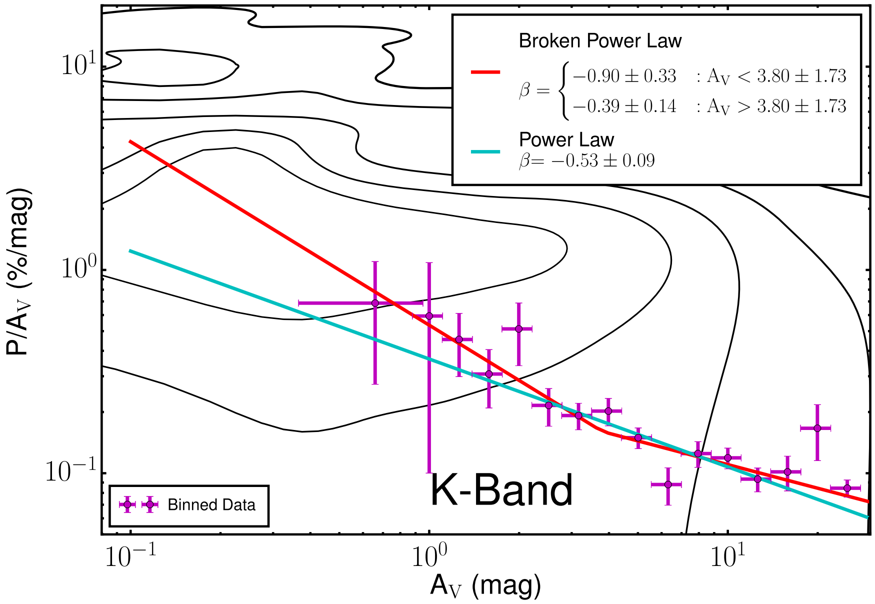

Figure 10. Same as Figure 7, but for *K*-band data. Bins with $A_V < 1.0$ mag were merged to further reduce the uncertainties.

and with a broken power law (hereafter, Model 2),

$$P_\lambda / A_V = \begin{cases} \alpha_1 A_V^{\beta_1} & : A_V \leqslant BP \\ \alpha_2 A_V^{\beta_2} & : A_V > BP \end{cases} \quad (3)$$

where $\alpha_2 = \alpha_1 BP^{\beta_1 - \beta_2}$. The four parameters α_1, β_1, and β_2, and BP were all taken as free parameters in the fit to Model 2.

The goodness-of-fit on the binned data to the two models was examined using the F-test and the bias-corrected Akaike information criterion (AICc, Akaike 1974; Sugiura 1978). The two different model comparison methods may exhibit different preferences. For example, Ludden et al. (1994) used Monte Carlo simulations to examine the performance of these methods, finding that the F-test tends to choose the simpler model more often than does the AICc, even when the more complex model is correct. To avoid possible bias, we used both methods to compare the model fits, and the preferred model was chosen to be the one for which (1) the F-test probability was below 0.05 (95% confidence level) and (2) had the lower AICc value. The results of the fitting and model comparisons are listed in Table 2. Both the F-test and AICc show consistent results; the broken power law is the better model for *H* bands, and the single power law is the better model for the R_c, i', and *K* bands.

The PE–A_V relations were empirically found to be insensitive to observing wavelengths (e.g., Andersson et al. 2015, and references therein), although our observed PE–A_V relations might be expected to show some differences among the observing bands, since each data set covered different A_V and spatial ranges. The R_c- and i'-band data mostly probed the regions with $A_V \lesssim 4$ mag, and thus the derived PE indices mainly characterize the low-A_V regions. The power index of −0.71 ± 0.10 for the R_c band is very different from the index

Table 2
Fitting Results for PE vs. A_V

Band	F-value	p-value	AICc	AICc	Preferred Model
	(model 1 →	model 2)	(model 1)	(model 2)	
R_c	0.30	0.75	22.30	30.00	$\mathrm{PE} = (0.86 \pm 0.12) A_V^{(-0.71 \pm 0.10)}$
i'	0.40	0.68	−5.64	5.74	$\mathrm{PE} = (1.66 \pm 0.17) A_V^{(-1.23 \pm 0.10)}$
H	3.95	0.04	40.68	39.92	$\mathrm{PE} = \begin{cases} (0.60 \pm 0.13) A_V^{(-0.95 \pm 0.30)} & : A_V < 2.88 \pm 0.67 \\ (0.29 \pm 0.07) A_V^{(-0.25 \pm 0.06)} & : A_V > 2.88 \pm 0.67 \end{cases}$
K	1.13	0.36	8.90	14.57	$\mathrm{PE} = (0.36 \pm 0.06) A_V^{(-0.53 \pm 0.09)}$

Note. The preferred model is determined by (1) a p value from the F-test below 0.05 (95% confidence level) or (2) a lower AICc value.

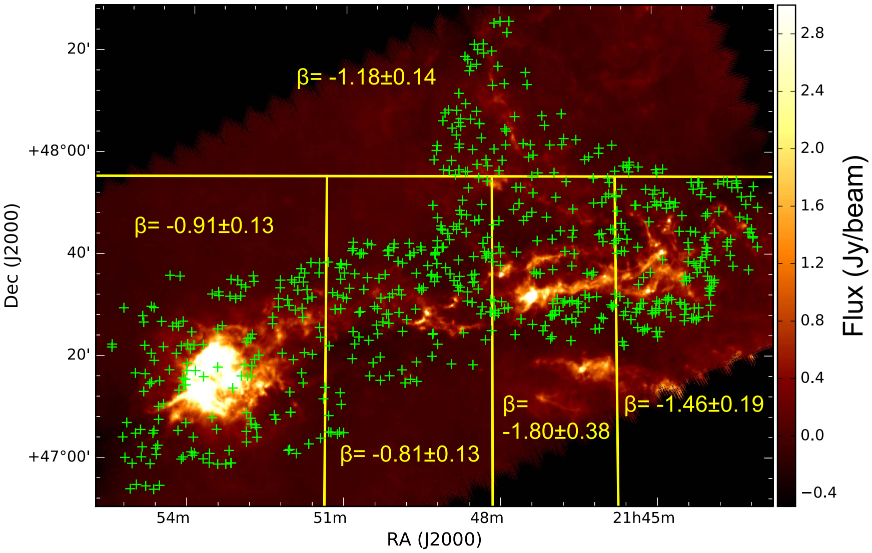

Figure 11. PE–A_V relations for the $A_V < 3$ mag stars in particular regions. The green crosses represent the stars with H-band polarization detections and $A_V < 3$ mag. These stars were separated into five zones, defined by the yellow lines, and the PE power-law β index was calculated for each zone by fitting a single power law. The β values vary with region from −0.81 ± 0.13 to −1.80 ± 0.38.

for the i' band, namely -1.23 ± 0.10. In addition, the power index of -0.95 ± 0.30 for the H band for low-A_V values is in between the indices for the R_c band and the i' band. For high-A_V regions, the index of -0.25 ± 0.06 for the H band is softer than the index for the K band (-0.53 ± 0.09), and both are flatter than all of the indices characterizing low-A_V regions. This finding may indicate that the physical properties of grains, as well as their alignment efficiencies, change significantly beyond $A_V \sim 3$–4 mag (see Section 5.4).

The R_c, i'-, and H-band data all covered the $A_V \lesssim 4$ mag regime; however, the power-law indices for these three bands were all different. One major difference between the R_c-, i'-, and H-band data was that the H-band observations covered almost all of the IC5146 cloud system, while the R_c-band observations mostly covered the main filament, and the i'-band observations only probed the northwest filament (see Figure 1).

To test whether the indices characterizing low-A_V regions differ from region to region, the stars with H-band detections and $A_V < 3$ mag were assigned to one of the five zones delineated in Figure 11. Within each zone, single power-law indices were derived, and they are shown in Figure 11. Power-law indices ranging from -0.81 ± 0.13 to -1.80 ± 0.38 were fit to the assigned H-band data within the different zones. The indices were significantly softer in the eastern part of the cloud than in the western and northern part. In addition, the index derived within the northern zone was -1.18 ± 0.14, nearly identical to the index for the i' band, namely -1.23 ± 0.06, covering a substantially similar region. Hence, the PE–A_V relation varies by region in the low-extinction regions. The different indices derived for the different wavelengths for the whole cloud could then merely arise from the combination of a variety of PE–A_V relations. The possible origin of the diverse PE relation is discussed further in Section 5.3.

4.3. Wavelength Dependence of Polarization using the Serkowski Relation

The polarization of starlight is known to be wavelength dependent, resulting in a polarization spectrum. Since this wavelength dependence originates from dust properties and alignment conditions, the polarization spectrum can be used to investigate the evolution of dust grains. The polarization spectrum is well-fit by the empirical "Serkowski relation,"

$$P(\lambda) = P_{\max} \cdot \exp\{-K \cdot \ln^2(\lambda_{\max}/\lambda)\}, \qquad (4)$$

where $P_{\max}$ is the peak polarization degree at wavelength $\lambda_{\max}$ (Serkowski 1973). In later studies, the parameter K was shown to follow the relation $K = -0.1 + c\lambda_{\max}$ (Wilking et al. 1982), where c was found to depend on dust properties, such as

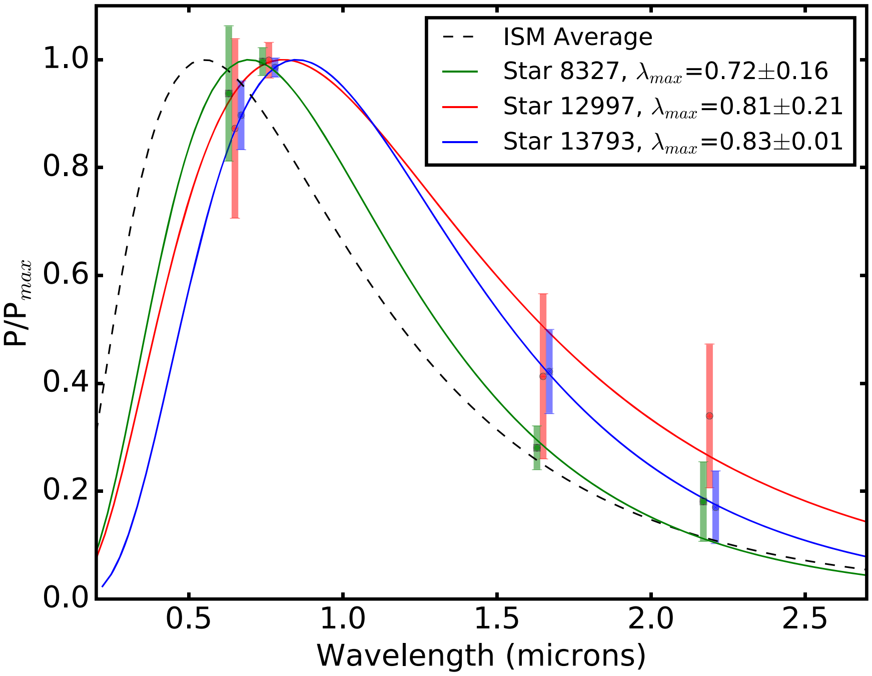

Figure 12. Polarization spectra for the three stars with polarization detections in four bands. Colored curves overplot the best-fit Serkowski relation. Wavelengths of the data points and error bars for stars 8327 and 13793 were slightly shifted to avoid overlapping. The black dashed spectrum represents the typical ISM average with $\lambda_{\rm max}$ of 0.55 μm. All three stars have higher $\lambda_{\rm max}$ values than the ISM average.

geometric shape (e.g., Voshchinnikov et al. 2013; Voshchinnikov & Hirashita 2014).

To fit the Serkowski relation for its three parameters, detections in at least four bands are required to obtain uncertainties in the parameters. However, it is difficult to do so in the presence of high extinction. Thus, most of the previous studies have been limited to low-extinction regions. Even in our data, only three stars were detected in all four wavebands. The Serkowski relation fit results for these stars are shown in Figure 12. The range of fitted $\lambda_{\rm max}$ is ~0.72–0.83 μm, significantly greater than the typical value ~0.55 μm characterizing the general diffuse interstellar medium (Serkowski et al. 1975).

4.4. *"Polarization Color" as a Constraint on λ_{max}*

It is difficult to obtain the necessary multiple wavelength polarization detections needed to fit Serkowski relations in the presence of strong extinction. In order to have more samples to constrain $\lambda_{\rm max}$, we examined the "polarization color" (the ratio of polarization degrees at two bands) as a partial descriptor of the polarization spectrum. Polarization color can be easily obtained from a limited set of wavebands without presumption of the spectrum shape. The Serkowski relation has been suggested to be only valid for a limited wavelength range, mostly UV through optical. Martin (1989) found that the polarization spectrum between 1.6 and 5 μm wavelength behaved more like a power law than like the Serkowski relation, and Clayton et al. (1992) found that the polarization spectrum in the ultraviolet showed an excess with respect to the Serkowski relation.

In the wavelengths where the Serkowski relation is valid, polarization color can constrain $\lambda_{\rm max}$. Following the Serkowski relation, the ratio of the polarization degree of a star at two wavelengths can be written as

$$\frac{P(\lambda_1)}{P(\lambda_2)} = \frac{\exp\{-K\cdot(\ln^2(\lambda_{\rm max}/\lambda_1))\}}{\exp\{-K\cdot(\ln^2(\lambda_{\rm max}/\lambda_2))\}}. \quad (5)$$

To reduce the free parameters, we also assumed the relation $K = -0.1 + c\lambda_{\rm max}$, where c is expected to be a constant over A_V. Via Equation (5) and the assumptions regarding K, the polarization color (ratio) is determined by only one free parameter, $\lambda_{\rm max}$. Thus, only one polarization color is required to constrain $\lambda_{\rm max}$, although for wavebands right near $\lambda_{\rm max}$, the uncertainties will be large. Clemens et al. (2016) used this approach with Mimir *H*- and *K*-band data to identify grain growth in the moderate- to high-extinction regions of L1544, finding $\lambda_{\rm max}$ in the 1.0–1.2 μm range.

The polarization color P_{R_c}/P_H versus A_V values shown in Figure 13 reveal how the polarization spectrum varies with A_V. The observed P_{R_c}/P_H distribution seems diverse and can hardly be described with a simple function. To try to find some order, we separated the stars into four A_V groups by eye, based on the similarities in the distribution. They span A_V ranges of <1, 1.0–2.5, 2.5–4.0, and >4.0 mag, labeled as regions A, B, C, and D, respectively. The blue horizontal lines show the unweighted average ± standard deviation (STD) of P_{R_c}/P_H for each group. The intrinsic dispersions of P_{R_c}/P_H were derived using $\sigma_{\rm intrinsic} = \sqrt{{\rm STD}^2 - \sigma_{\rm obs}^2}$, where $\sigma_{\rm obs}$ was the average observational uncertainty. The statistical properties of P_{R_c}/P_H for each group are presented in Table 3.

Group A had significantly lower mean P_{R_c}/P_H than the other regions. Since the A_V of this region was comparable to the expected foreground extinction <0.3 mag (Lada et al. 1994), the depolarization due to any foreground medium might significantly affect the polarization spectrum. Thus, the polarization color in this group might not accurately trace the dust properties. The average P_{R_c}/P_H values for groups B, C,

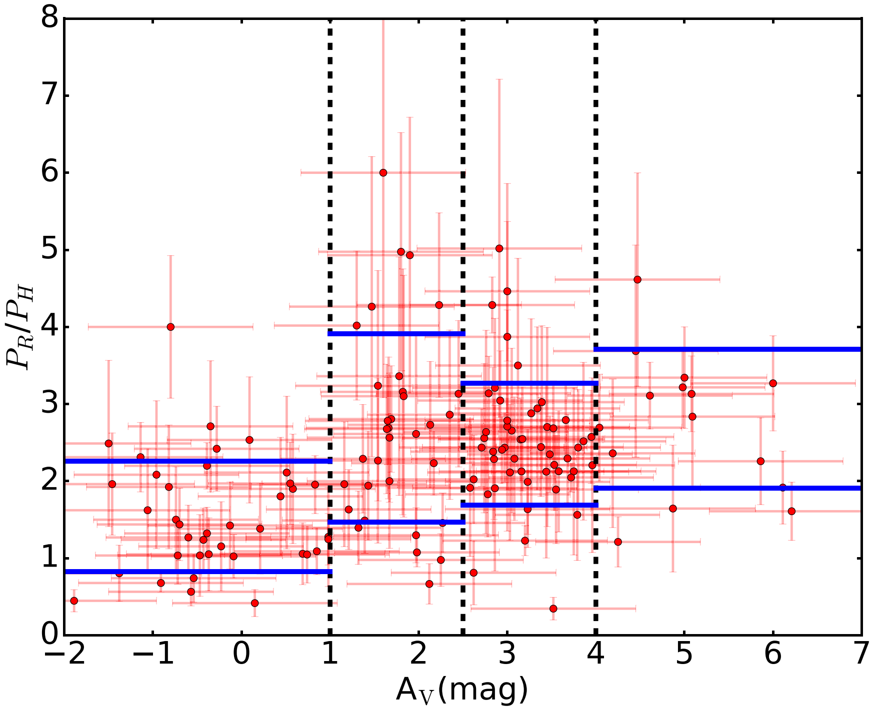

Figure 13. P_{R_c}/P_H vs. A_V from the stars with R_c- and H-band polarization detections. These stars were separated into four groups, based on their A_V values as defined by the black dashed lines. The blue horizontal lines show the $\pm 1\sigma$ excursions above and below the average of P_{R_c}/P_H for each group. The distribution of P_{R_c}/P_H is narrowest when $A_V = 2.5$–4 mag. The stars with negative A_V values have negligible extinction: these values result from uncertainties in the NICER extinction estimation.

Table 3
Variation of P_{R_c}/P_H with A_V

Group	A_V Range (mag)	P_{R_c}/P_H				$\langle\lambda_{\max}\rangle$ [a] (μm)
		Mean	STD	σ_{obs}	Intrinsic Dispersion[b]	
A	−2.0–1.0	1.54 ± 0.09	0.72 ± 0.11	0.53	0.54 ± 0.15	0.92 ± 0.02
B	1.0–2.5	2.69 ± 0.20	1.22 ± 0.30	0.97	0.73 ± 0.50	0.75 ± 0.03
C	2.5–4.0	2.48 ± 0.12	0.79 ± 0.17	0.80	…	0.78 ± 0.02
D	>4.0	2.81 ± 0.22	0.90 ± 0.29	0.78	0.44 ± 0.59	0.73 ± 0.03

Notes.
[a] The $\lambda_{\max}$ calculated from the mean P_{R_c}/P_H. Uncertainties were calculated from the means and the propagated uncertainties of the means, assuming $c = 2.3$.
[b] The intrinsic dispersions and the uncertainties of the dispersions. The intrinsic dispersion cannot be defined if the observed dispersion is lower than the instrumental uncertainty.

and D were similar to each other, although significant intrinsic dispersion was found for group B.

The value of P_{R_c}/P_H directly determines the value of $\lambda_{\max}$ if the parameter c in Equation (5) is known. The variance-weighted mean c of 2.3 was derived from the four-band fitting to the three stars shown in Figure 12. This c value was higher than the value of 1.66 found in Wilking et al. (1982) and the value of 1.86 found in Whittet et al. (1992). Figure 14 shows how P_{R_c}/P_H maps to $\lambda_{\max}$ for different value of c. The black horizontal dashed lines delimit the span of the distribution of P_{R_c}/P_H values found in Figure 13. The curves in Figure 14 characterized by $c \leqslant 2.1$ cannot cover the full range of the distribution of observed P_{R_c}/P_H values, suggesting that the parameter c value in the IC5146 cloud system is likely higher than it is in other clouds. Hence, we assumed $c = 2.3$ to estimate the $\lambda_{\max}$ from observed P_{R_c}/P_H.

The range of $\lambda_{\max}$ versus A_V, for $c = 2.3$, is shown in Figure 15. The mean $\lambda_{\max}$ for the mean P_{R_c}/P_H in each of the four A_V groups is listed in Table 3. For each P_{R_c}/P_H, two possible $\lambda_{\max}$ solutions from the Serkowski relation are possible, as can been seen in Figure 14. These two solution regions were colored in gray for the lower $\lambda_{\max}$ values and in red for the greater $\lambda_{\max}$ values. If we assume that $\lambda_{\max}$ across the cloud system does not dramatically change within a few magnitudes of extinction, then only one set of solutions is likely to be true. Since the values of $\lambda_{\max}$ derived from the four-band fitting to the three stars shown in Figure 12 were all in the range of 0.72–0.83 μm, $\lambda_{\max} > 0.4\ \mu$m selects the better solutions.

Hence, the average P_{R_c}/P_H values correspond to $\lambda_{\max}$ of 0.75, 0.78, and 0.73 μm for groups B, C, and D, respectively. These $\lambda_{\max}$ are all greater than the average value for the ISM of 0.55 μm (Serkowski et al. 1975), suggesting that the dust grains across most of the IC5146 cloud system have grown significantly with respect to dust grains in the diffuse ISM. In addition, the large dispersion of $\lambda_{\max}$ in group B implies that

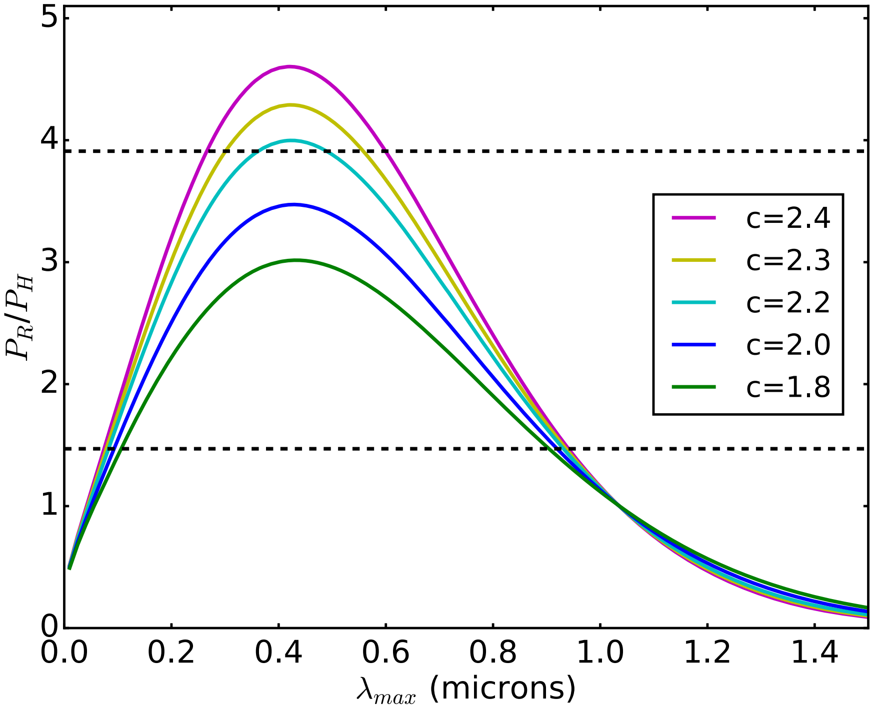

Figure 14. Relations between P_{R_c}/P_H and $\lambda_{\rm max}$ predicted by the Serkowski relation assuming $K = c\lambda_{\rm max}$. The horizontal dashed lines represent the range of observed P_{R_c}/P_H, seen as the range spanned by the blue horizontal lines shown in Figure 13. Only the relation characterized by $c \geqslant 2.2$ can cover the range of observed P_{R_c}/P_H. The yellow curve shows the relation for $c = 2.3$, which was used to convert P_{R_c}/P_H into $\lambda_{\rm max}$.

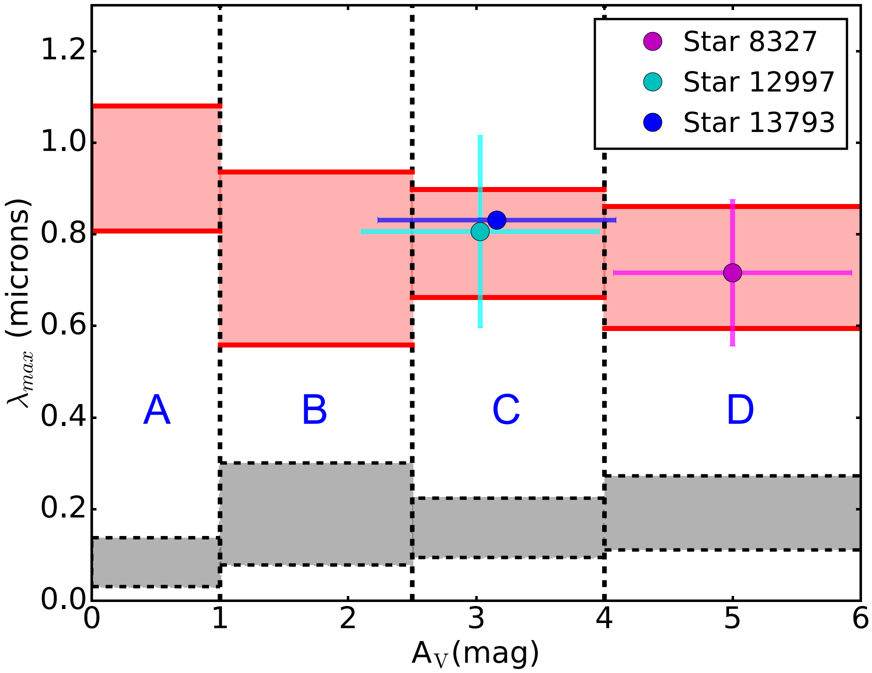

Figure 15. Ranges of $\lambda_{\rm max}$ with A_V group. The colored regions represent the ranges of the distributions of $\lambda_{\rm max}$ values in each A_V group, estimated from the observed P_{R_c}/P_H values, the Serkowski relation, and the $c = 2.3$ curve from Figure 14. The red and gray sets of zones identify the two degenerate sets of solutions to the Serkowski relation. The three stars whose four-band polarimetry data were fitted to the Serkowski relation (see Figure 12) are plotted as filled colored circles with error bars and are consistent with the set of red zone solutions corresponding to greater values of $\lambda_{\rm max}$.

the dust grain size distributions are more diverse in this A_V range than in the other extinction regions.

Similarly, we plot P_H/P_K versus A_V in Figure 16 to trace the variation in polarization spectrum in the infrared. The data were separated into five groups, in a fashion similar to Figure 13 (A_V < 1, 1.0–2.5, 2.5–4.0, 4.0–10.0, and >10.0 mag, labeled as A, B, C, D, and E, respectively). The statistical properties of P_H/P_K for these groups are listed in Table 4. The average P_H/P_K changes significantly with A_V, with the greatest value found in group B.

The values of $\lambda_{\rm max}$ converted from P_H/P_K were listed in Table 4. The range of $\lambda_{\rm max}$ derived from the group averaged

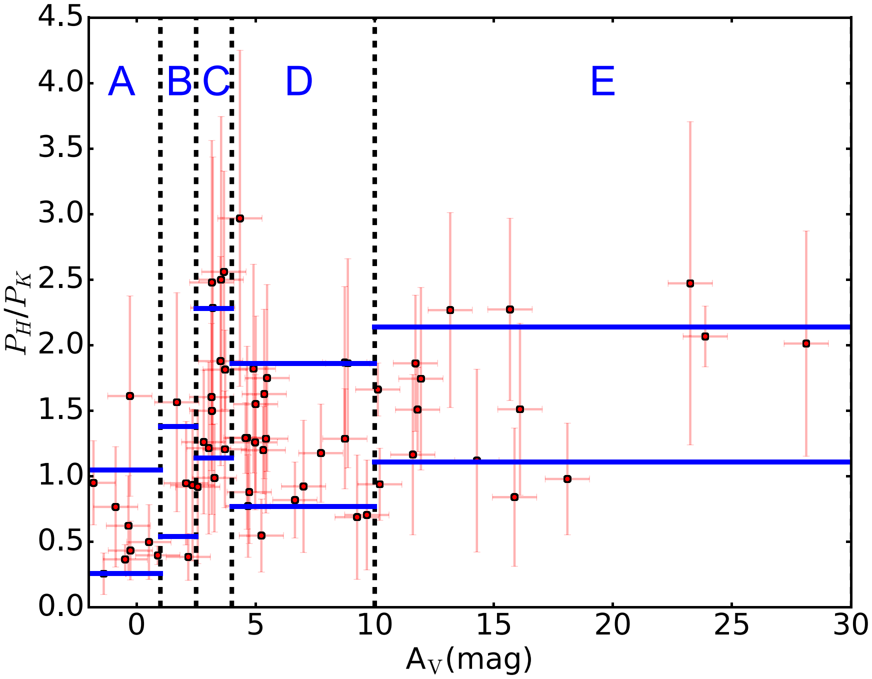

Figure 16. Same as Figure 13, but for P_H/P_K vs. A_V. The dispersions of P_H/P_K are almost the same over the different A_V groups, while the P_H/P_K means appear to change with A_V.

Table 4
Variation of P_H/P_K with A_V

Group	A_V Range (mag)	P_H/P_K Mean	STD	$\sigma_{\rm obs}$	Intrinsic Dispersion[b]	$\langle\lambda_{\rm max}\rangle$[a] ($\mu$m)	Power-law Index
A	−2.0–1.0	0.66 ± 0.12	0.39 ± 0.21	0.31	0.27 ± 0.30	$2.20^{+0.13}_{-0.12}$	−1.38 ± 0.60
B	1.0–2.5	0.96 ± 0.20	0.42 ± 0.31	0.52	⋯	$1.93^{+0.17}_{-0.15}$	−0.14 ± 0.69
C	2.5–4.0	1.71 ± 0.21	0.57 ± 0.24	0.72	⋯	$1.40^{+0.14}_{-0.13}$	1.78 ± 0.41
D	4.0–10.0	1.31 ± 0.13	0.54 ± 0.20	0.54	⋯	$1.67^{+0.09}_{-0.08}$	0.90 ± 0.33
E	>10.0	1.63 ± 0.16	0.51 ± 0.19	0.58	⋯	$1.46^{+0.11}_{-0.11}$	1.62 ± 0.33

Notes.

[a] The $\lambda_{\rm max}$ calculated from the mean P_{R_c}/P_H. Uncertainties were calculated from the means and the propagated uncertainties of the means, assuming $c = 2.3$.

[b] The intrinsic dispersions and the uncertainties of the dispersions. The intrinsic dispersion cannot be defined if the observed dispersion is lower than instrumental uncertainty.

P_H/P_K was 1.46–1.93 μm, significantly higher than the 0.73–0.78 μm range derived from P_{R_c}/P_H. The inconsistency implies that the Serkowski relation may not describe the polarization spectrum at near-infrared wavelengths well. Martin (1989) suggested that the near-infrared polarization spectrum can be better described by a power law

$$P(\lambda) \propto \lambda^{-\beta}, \tag{6}$$

where $\beta \simeq 1.6$–2.0. In the infrared, polarization color can still constrain the power-law index by

$$\frac{P_H}{P_K} = 0.74^{-\beta}. \tag{7}$$

The β derived from our data are listed in Table 4. These indices probably vary with A_V and have a peak at $A_V \approx 2.5$–4 mag, as shown by Figure 16. Kim & Martin (1995) showed that the index could depend on the amount of micron-sized dust grains. Our results indicate that the population of micron-sized dust grains might evolve with A_V, and a significant change occurs at A_V of 2.5–4 mag.

5. Discussion

5.1. Evolution of Dust Grains

The derived $\lambda_{\rm max}$ values obtained in previous studies (e.g., Whittet & van Breda 1978; Wilking et al. 1982) are expected to be related to the small-size cutoff of the grain size distribution. Whittet & van Breda (1978) found that $\lambda_{\rm max}$ is related to the ratio of total to selective extinction ($R_V = A_V/(E_{B-V})$) by an empirical relation $R_V = (5.6 \pm 0.3)\,\lambda_{\rm max}$, tracing the reddening changes with grain size distribution changes. However, with more observations, Andersson & Potter (2007) found no correlation between $\lambda_{\rm max}$ and R_V for individual clouds; the empirical relation could only be recovered by combining the data for all of their observed clouds. They further argued that $\lambda_{\rm max}$ may depend on both grain size distributions and dust alignment conditions.

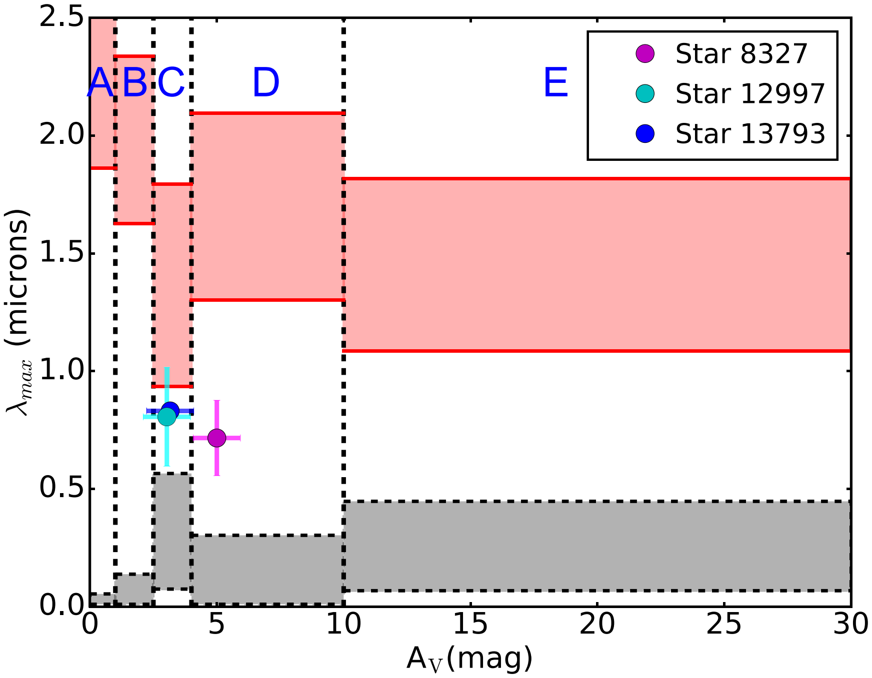

Figure 17. (a) Same as Figure 15, but the $\lambda_{\rm max}$ range was estimated from P_H/P_K using the Serkowski relation with $c = 2.3$. The $\lambda_{\rm max}$ values derived from P_H/P_K are much greater than the $\lambda_{\rm max}$ values derived from P_{R_c}/P_H shown in Figure 15. In addition, the distribution of $\lambda_{\rm max}$ is inconsistent with the best-fit Serkowski relations to the three stars with four-band polarimetry data shown in Figure 12, suggesting that the Serkowski relation may not be valid, at least in the K band.

Whittet et al. (2008) showed in their RATs simulations with constant grain size distribution that $\lambda_{\rm max}$ increases with A_V because small dust grains become less well aligned as a result of the decaying and reddening of the external radiation field by extinction. Their model predicts a smooth increase of $\lambda_{\rm max}$ from 0.45 to 0.75 μm as A_V increases from 0 to 6 mag. However, our derived $\lambda_{\rm max}$ values, 0.73–0.78 μm, do not significantly change with A_V. In addition, our data show a significant decrease of the intrinsic dispersion of $\lambda_{\rm max}$ from 0.11 ± 0.08 ($A_V =$ 1.0–2.5 mag) to <0.07 ($A_V =$ 2.5–4.0 mag), possibly due to changes of the grain size distribution.

The change in the dispersion of $\lambda_{\rm max}$ implies that the grain size distribution in the dense regions could be more uniform than in the diffuse regions. We speculate that the difference is due to the evolution of the dust grain size. In grain-grain collision models (Jones et al. 1996; Hirashita & Yan 2009; Ormel et al. 2009), the grain size distributions are expected to be modified by the competing effects of fragmentation and coagulation. Steady-state grain size distributions are eventually reached when these two effects achieve equilibrium. As a result, the apparent uniform grain size distribution in the dense regions may indicate the existence of stabilized grain-grain collision processes. Together with the increase of $\lambda_{\rm max}$, this non-evolution of grains in the dense regions favors the notion that grain growth has already taken place before A_V reaches 2.5–4.0 mag.

In Figure 17 we show that the $\lambda_{\rm max}$ derived from a Serkowski relation based on an analysis of P_H/P_K yielded an average $\lambda_{\rm max}$ of 1.46–1.93 μm. This was inconsistent with $\lambda_{\rm max}$ derived from P_{R_c}/P_H, which yielded an average $\lambda_{\rm max}$ of 0.73–0.78 μm. To reach a $\lambda_{\rm max}$ of 0.73–0.78 μm, P_H/P_K would need to be >2.3, which is much higher than the observed range of mean values from 0.96 ± 0.28 to 1.71 ± 0.21. This indicates that at least the measured K-band infrared polarization exceeds the predictions of the Serkowski relation. This excess infrared polarization was also found in early studies (e.g., Jones 1990; Martin & Whittet 1990; Nagata 1990) and is better fit by a power law (Equation (7)). We found that a power law with β ranging from -0.14 ± 0.69 to 1.78 ± 0.41 can explain our data for different A_V. The β index appears to vary with A_V and has its highest value for $A_V =$ 2.5–4.0 mag. Our β are similar to, or smaller than, the value of 1.6 ± 0.2 measured toward ScO-Oph and CyG OB2 (Martin et al. 1992), and 1.76 ± 0.25 measured toward the Galactic center (Hatano et al. 2013).

Two models have tried to explain the physical origin of the excess infrared polarization over the Serkowski relation. Kim & Martin (1995) showed that a model with a dust grain mixture with sizes of 0.3 μm and 0.6–1 μm can reproduce the observational Serkowski relation while also exhibiting a power-law excess infrared polarization. Li & Greenberg (1997) showed that an organic refractory-mantled dust grain model with a Gaussian grain size distribution could reproduce the observed excess infrared polarization without requiring a high abundance of micron-sized dust grains. Our results show that the observed power-law index might vary with A_V, providing new constraints for future models.

5.2. How Deep Into a Cloud Can Polarization Be Used to Reveal B fields?

PE has been used to indicate how deep into a cloud, in A_V, the dust grains remain aligned. Goodman et al. (1995) found a PE–A_V power-law index of −1 in L1755 in the *JHK* bands. This constancy of P with A_V was used to argue that near-infrared polarization does not trace the B field within dense clouds. In contrast, Whittet et al. (2008) found an index of −0.52 in Taurus at the K band, showing that polarization can trace the B field, at least up to $A_V \sim 10$ mag.

The power-law PE versus A_V indices characterizing these two cases can be found in our data, but for different A_V ranges. The power index of -0.95 ± 0.30 measured for the H band in low-A_V regions is similar to the results found in L1755 at the R band (Goodman et al. 1995) for $A_V <$ 8–10 mag. Our index of -0.53 ± 0.09 for the K band is close to the value found in Taurus at the K band (-0.52 ± 0.07) by Whittet et al. (2008) and the value found in numerous starless cores at the K band (~ -0.5) for $A_V < 20$ mag by Jones et al. (2015). In addition, the intermediate index -0.71 ± 0.10 found in the R_c band is similar to the results found in Pipe-109 using the R band (-0.76 ± 0.14, Alves et al. 2014) and in L204 using the H band (-0.74 ± 0.07, Cashman & Clemens 2014). We found our steepest index, of -1.23 ± 0.10, in the i' band and our softest index, of -0.25 ± 0.06, in the H band in high-A_V regions.

The softer indices of -0.25 to -0.53 are only found in high-A_V regions in the H and K bands, while a variety of steeper indices are found in low-A_V regions. The ~ -0.5 indices match predictions of RATs models with constant grain size distributions (Whittet et al. 2008). The same models predicts a steepening of PE as A_V approaches 10 mag, caused by the strong extinction of external radiation. Here, however, the indices we measure for high-A_V regions show that the dust with A_V up to $\sim$20 mag still contributes to the measured polarization: the PE at $A_V = 20$ mag is only a factor of $\sim$2 lower than that at $A_V = 4$ mag. Thus, the notion that only the dust on the surfaces of clouds is aligned, as concluded by Goodman et al. (1995), is not supported here.

5.3. The Diverse PE in Low-A_V Regions

It is interesting that a variety of PE versus A_V power-law behaviors are seen across the IC5146 cloud system. We showed that the indices derived using the H band varied with region location in Figure 11. The diverse PE–A_V relations likely depend more on A_V and region choice and less on wavelength, as the indices derived from i' and H bands in the same region are almost the same. If all the stellar values from all of the low-A_V regions are combined into a single plot and fitted, the location dependence of the PE–A_V relation would be mixed and thereby lost. The index of -0.95 derived from the H band using all data with low-A_V is merely the average from the mixed PE–A_V relation shown in Figure 11. This is different from the suggestion by Goodman et al. (1995) that a power-law index of ~ -1 indicates that starlight polarization only traces the dust grains on the surfaces of clouds.

Three possibilities could explain the origin of the wide variation of the PE–A_V relation.

(i) The grain size distributions could be diverse and vary greatly from region to region for low A_V. In Section 4.3 we showed that the dispersion of $\lambda_{\max}$, estimated from P_{R_c}/P_H, is significantly larger for $A_V < 2.5$ mag, suggesting that grain size distributions are diverse. This diversity is likely region-dependent, since the different $\lambda_{\max}$ values were derived from different sightlines. The grain size distribution is a key element of the RATs theory; radiation can efficiently align dust grains with sizes comparable to its wavelength, and wavelength determines radiation penetration ability.

(ii) Depolarization effects may occur if multiple polarizing layers exist. In Figure 11 we showed that the PE versus A_V indices derived in the western part of the IC5146 cloud were steeper than -1, hence the polarization percentage must decrease with A_V. This may be a result of depolarization. If a multiple layer structure, in which the layers have different B-field orientations, exists along a line of sight, the net transferred polarization from the different layers would be reduced. Arzoumanian et al. (2011) found rich and hierarchical filamentary structure in the IC5146 cloud system. These filaments can naturally produce a multiple layer structure if the projections of such structures overlap along the line of sight. In addition, they further found that most of the filaments in the western part of the IC5146 cloud system were supercritical, which might twist to cause complex B fields. This could explain the steeper indices found in the western part of the cloud.

(iii) The degree of dust alignment may be affected by one or more bright illuminators, such as the stars in the Cocoon Nebula. Cashman & Clemens (2014) found a possible dependence of PE–A_V index for regions in the L204 cloud 3 with distance from a nearby illuminator. Brighter stellar radiation can boost alignment of the dust, and the alignment efficiency will mainly depend on the optical depth to the illuminator. In IC5146, the Cocoon Nebula stellar cluster could be a strong illuminator that is able to affect grain alignment. However, the radiation from the Cocoon Nebula is also highly shadowed by the main filament structure, making the optical depth from the Cocoon Nebula to the other regions difficult to estimate.

5.4. The Breakpoint in PE–A_V Relations

In Section 4.2 we showed that PE decays with A_V and a breakpoint (BP) of $A_V = 2.88 \pm 0.67$ mag separates two different power-law slopes of A_V in the H band. Breakpoints of PE near $A_V \sim$ 2–3 mag are rarely seen. Pipe-109 shows a breakpoint at 9.5 mag with power index changing from -1.00 to -0.34 (Alves et al. 2014). LDN 183 shows a breakpoint at $A_V \sim 20$ mag with power index changing from -0.6 to -1 (Crutcher 2004; Clemens 2012; Andersson et al. 2015). Jones et al. (2015) also found a break point at $A_V \sim 20$ mag with power index changing from -0.5 to -1 toward several starless cores. Jones et al. (2016) found an break point at very high A_V, $\sim$hundreds mag in the Class 0 YSO G034.43+00.24 MM1 with a change of power index from -1 to -0.5.

Three mechanisms could change the power-law indices with A_V, although in opposite directions. Radiation into the deepest regions could be too faint to align the dust grains, so the power-law index for high-A_V regions should steepen (Whittet et al. 2008). If grains grow at higher A_V, however, the alignment efficiency will be higher for dust with sizes comparable to the wavelength (Lazarian & Hoang 2007), hence the power-law index will become flatter in the dense regions where only radiation with longer wavelengths can penetrate and the dust grains are believed to grow. In addition to the change of dust properties, internal radiation fields from embedded sources within dense clouds could also enhance dust alignment and flatten the power-law index.

Andersson et al. (2015) suggested that the origin of the breakpoint found in LDN 183 is likely due to the extinction of external radiation because their power-law index in low-A_V regions, of -0.6, is consistent with prediction of the RATs model assuming constant grain size (Whittet et al. 2008). Similar trends were also found within several starless cores by Jones et al. (2015), and they further showed that the RATs theory can explain the break point of $\sim$20 mag, where the dust optical depth, for the wavelength comparable to the maximum grain size, becomes optically thick.

Our results showed an opposite trend as compared to the case of LDN183: steeper indices ranging from -0.71 to -1.23

were found in low-A_V regions, while flatter indices ranging from −0.25 to −0.53, consistent with the Whittet et al. (2008) model, were found in high-A_V regions for all observed wavebands. The results from Alves et al. (2014) toward Pipe-109 and Jones et al. (2016) in G034.43+00.24 MM1 show similar trends as ours, but with different breakpoints. The flattened slopes in high-A_V regions more likely originate from efficient grain alignment due to either grain growth or internal radiation fields. Because Pipe-109 is a starless object but G034.43+00.24 MM1 is a Class 0 YSO, the change of slope for the former likely results mainly from grain growth, while internal radiation might play an important role in the latter. Since the breakpoint of $A_V \sim 2.8$ mag shown in our data is consistent with the A_V of the regions where the intrinsic dispersion of $\lambda_{\max}$ drops significantly ($A_V = 2.5$–4.0 mag), our observed trend is more likely caused by grain growth.

An open question is why the breakpoint we measure is so different from the 9.5 mag value in Alves et al. (2014), although both breakpoints likely result from grain growth. The difference could originate from two possible reasons. First, Alves et al. (2014) lacked samples in low-A_V regions, and thus a broken power law with breakpoint at $A_V \sim 3$ mag would be difficult to identify. Second, the difference may come from different grain growth conditions. Ormel et al. (2009) simulated the evolution of dust grain size, based on grain-grain collisions. They found that dust grains with ice-coatings are more likely to aggregate and grow than are grains without ice-coatings, due to the increased surface stickiness. Chiar et al. (2011) found that H_2O-ice in IC5146 only exists in regions exhibiting extinctions exceeding $A_V \sim 4$ mag, a value quite similar to the breakpoint we found. Thus, H_2O-ice mantling could induce a breakpoint via enhanced grain growth. Similarly, Whittet et al. (2001) found that the observed R_V in Taurus changed from $R_V \sim 3$ to 4 around $A_V = 3.2$ mag, coincident with the extinction threshold for H_2O-ice mantling in Taurus, and suggested that mantle growth is an important process in initial grain growth. We conclude that such mantling also enables greater efficiency of dust grain alignment, permitting magnetic field to be traced deeper into clouds than if such mantling is not present.

6. Conclusions

We performed optical and infrared polarimetry observations toward background stars seen through the IC5146 dark cloud system using AIMPOL at the ARIES Observatory, TRIPOL at the Lulin Observatory, and Mimir at the Lowell Observatory Perkins Telescope. A total of 2022 stars showed significant polarization detection in at least one of the four wavebands observed. From the analysis of these data, we found the following results.

1. The polarization efficiency (PE $\equiv P_\lambda / A_V$) decreases with A_V as a power law or broken power law. The values of the power-law indices likely depend more on the choice of targeted regions and local extinction, and less on observing wavelength.
2. A cloud-averaged power-law index of −0.95 for PE versus A_V was found in the H band for low A_V, the same as the index found in L1755 by Goodman et al. (1995). However, we showed that the index of −0.95 resulted from the admixture of a variety of PE–A_V relations, whose local-regional indices varied from −0.8 to −1.8, different from the suggestion by Goodman et al. (1995) that the index of ~ -1 indicates that background starlight polarization only traces the dust grains on the surface of clouds.
3. A broken power law relation for PE versus A_V in the H band exhibits a breakpoint at about $A_V \sim 2$–3 mag. The power-law index in high-A_V regions is shallow and consistent with predictions from RATs models (Whittet et al. 2008), while the indices in low-A_V regions are steeper and vary with region. The shallow index in high-A_V regions is likely due to grain growth.
4. Excess infrared polarization, over that predicted by the Serkowski relation, was observed in P_H / P_K, possibly resulting from abundance enhancements of large micron-sized dust grains. The average P_H / P_K varies with A_V from 0.96 ± 0.20 to 1.71 ± 0.21, and exhibits its highest value of 1.71 ± 0.21 for A_V in the 2.5–4.0 mag range. This implies that the abundance of such micron-sized dust grains might change with A_V.
5. The polarization color (P_{R_c}/P_H) is a useful tool to constrain $\lambda_{\max}$, the peak of the Serkowski relation, which may trace the small-size cutoff of the grain size distribution. We found that both the average and dispersion of P_{R_c}/P_H decreased from the $1.0 < A_V < 2.5$ mag range to the $2.5 < A_V < 4.0$ mag range. These variations suggest that the small-size cutoffs of grain size distributions are most likely due to efficient grain-grain collisions, and thus indicate that grain growth could already take place by $A_V \sim 2.5$–4.0 mag, possibly enhanced at this relatively low-A_V range by the presence of ice mantles on the grains.

In conclusion, this study revealed that dust grains in the diffuse molecular regions ($A_V < 2.5$ mag) of the IC5146 dark cloud system have diverse size distributions. As A_V approaches ∼3 mag, submicron dust grains grow significantly due to grain-grain collisions. The size distributions may also become more uniform as A_V increases as a balance is reached between fragmentation and coagulation. In addition, the larger micron-sized grains likely already exist in the diffuse regions, and their abundances and sizes likely change with A_V. In the next paper of this series, we will use these polarization data to characterize the magnetic field morphology and strength across this system of filamentary dark molecular clouds associated with IC5146.

We acknowledge support from the Aryabhatta Research Institute of Observational Sciences and Lulin Observatory concerning the data collected using AIMPOL and TRIPOL. This research was conducted in part using the Mimir instrument, jointly developed at Boston University and Lowell Observatory and supported by NASA, NSF, and the W.M. Keck Foundation. This work and the analysis software for Mimir data were developed under NSF grants AST 06-07500, 09-07790, and 14-12269 to Boston University. We thank Brian Taylor, Tao-Chung Ching, and Lauren Cashman for their help in the smooth operations of Mimir observations. This research has made use of the Herchel Science Archive (HSA), and the data are based on the observations performed with the ESA *Herschel* Space Observatory (Pilbratt et al. 2010). J.W.W., S.P.L., and C.E. are grateful for the support from the Ministry of Science and Technology (MOST) of Taiwan through grants NSC 99-2923-M-008-002-MY3, NSC 101-2119-M-007-004, MOST 102-2119-M-007-004-MY3, 105-2119-M-007-022-MY3, and 105-2119-M-007-024.

Facilities: ARIES:ST, LO:1m, Perkins.

Software: IRAF, Source Extractor (Bertin & Arnouts 1996), Mimir Software Package (Clemens et al. 2012c), PNICER (Meingast et al. 2017), Astropy (Astropy Collaboration et al. 2013), NumPy (van der Walt et al. 2011), SciPy (Jones et al. 2001), Aplpy (Robitaille & Bressert 2012).

ORCID iDs

Jia-Wei Wang https://orcid.org/0000-0002-6668-974X
Shih-Ping Lai https://orcid.org/0000-0001-5522-486X
Chakali Eswaraiah https://orcid.org/0000-0003-4761-6139
Dan P. Clemens https://orcid.org/0000-0002-9947-4956
Wen-Ping Chen https://orcid.org/0000-0003-0262-272X

References

Akaike, H. 1974, ITAC, 19, 716
Alves, F., Frau, P., Girart, J. M., et al. 2014, A&A, 569, A1
Andersson, B.-G., Lazarian, A., & Vaillancourt, J. E. 2015, ARA&A, 53, 501
Andersson, B.-G., & Potter, S. B. 2007, ApJ, 665, 369
Arzoumanian, D., André, P., Didelon, P., et al. 2011, A&A, 529, L6
Astropy Collaboration, Robitaille, T. P., Tollerud, E. J., et al. 2013, A&A, 558, A33
Bertin, E., & Arnouts, S. 1996, A&AS, 117, 393
Cashman, L. R., & Clemens, D. P. 2014, ApJ, 793, 126
Chapman, N. L., Goldsmith, P. F., Pineda, J. L., et al. 2011, ApJ, 741, 21
Chiar, J. E., Pendleton, Y. J., Allamandola, L. J., et al. 2011, ApJ, 731, 9
Cho, J., & Lazarian, A. 2005, ApJ, 631, 361
Clayton, G. C., Anderson, C. M., Magalhaes, A. M., et al. 1992, ApJL, 385, L53
Clemens, D. P. 2012, ApJ, 748, 18
Clemens, D. P., Pavel, M. D., & Cashman, L. R. 2012a, ApJS, 200, 21
Clemens, D. P., Pinnick, A. F., & Pavel, M. D. 2012b, ApJS, 200, 20
Clemens, D. P., Pinnick, A. F., Pavel, M. D., & Taylor, B. W. 2012c, ApJS, 200, 19
Clemens, D. P., Sarcia, D., Grabau, A., et al. 2007, PASP, 119, 1385
Clemens, D. P., Tassis, K., & Goldsmith, P. F. 2016, ApJ, 833, 176
Crutcher, R. M. 2004, Ap&SS, 292, 225
Davis, L., Jr., & Greenstein, J. L. 1951, ApJ, 114, 206
Dolginov, A. Z., & Mitrofanov, I. G. 1976, Ap&SS, 43, 291
Draine, B. T., & Weingartner, J. C. 1996, ApJ, 470, 551
Draine, B. T., & Weingartner, J. C. 1997, ApJ, 480, 633
Eswaraiah, C., Pandey, A. K., Maheswar, G., et al. 2011, MNRAS, 411, 1418
Eswaraiah, C., Pandey, A. K., Maheswar, G., et al. 2012, MNRAS, 419, 2587
Goodman, A. A., Jones, T. J. B., Lada, E. A., & Myers, P. C. 1995, ApJ, 448, 748
Griffin, M. J., Abergel, A., Abreu, A., et al. 2010, A&A, 518, L3
Hall, J. S. 1949, Sci, 109, 166
Hatano, H., Nishiyama, S., Kurita, M., et al. 2013, AJ, 145, 105
Heiles, C. 2000, AJ, 119, 923
Hiltner, W. A. 1949a, ApJ, 109, 471
Hiltner, W. A. 1949b, Sci, 109, 165
Hirashita, H., & Yan, H. 2009, MNRAS, 394, 1061
Hoang, T., & Lazarian, A. 2009, ApJ, 695, 1457
Indebetouw, R., Mathis, J. S., Babler, B. L., et al. 2005, ApJ, 619, 931
Jones, A. P., Tielens, A. G. G. M., & Hollenbach, D. J. 1996, ApJ, 469, 740
Jones, E., Oliphant, E., Peterson, P., et al. 2001, SciPy Open Source Scientific Tools for Python (http://www.scipy.org)
Jones, R. V., & Spitzer, L., Jr. 1967, ApJ, 147, 943
Jones, T. J. 1990, AJ, 99, 1894
Jones, T. J., Bagley, M., Krejny, M., Andersson, B.-G., & Bastien, P. 2015, AJ, 149, 31
Jones, T. J., Gordon, M., Shenoy, D., et al. 2016, AJ, 151, 156
Kim, S.-H., & Martin, P. G. 1995, ApJ, 444, 293
Lada, C. J., Alves, J., & Lada, E. A. 1999, ApJ, 512, 250
Lada, C. J., Lada, E. A., Clemens, D. P., & Bally, J. 1994, ApJ, 429, 694
Lazarian, A., Goodman, A. A., & Myers, P. C. 1997, ApJ, 490, 273
Lazarian, A., & Hoang, T. 2007, MNRAS, 378, 910
Li, A., & Greenberg, J. M. 1997, A&A, 323, 566
Li, H.-b., Fang, M., Henning, T., & Kainulainen, J. 2013, MNRAS, 436, 3707
Lombardi, M., & Alves, J. 2001, A&A, 377, 1023
Ludden, T. M., Beal, S. L., & Sheiner, L. B. C. 1994, Journal of Pharmacokinetics and Biopharmaceutics, 22, 431
Martin, P. G., Adamson, A. J., Whittet, D. C. B., et al. 1992, ApJ, 392, 691
Martin, P. G., & Whittet, D. C. B. 1990, ApJ, 357, 113
Martin, P.G. 1989, in IAU Symp. 135, Interstellar Dust, ed. L. J. Allamandola & A. G. G. M. Tielens (Dordrecht: Kluwer), 55
Meingast, S., Lombardi, M., & Alves, J. 2017, A&A, 601, A137
Nagata, T. 1990, ApJL, 348, L13
Ormel, C. W., Paszun, D., Dominik, C., & Tielens, A. G. G. M. 2009, A&A, 502, 845
Parzen, E. 1962, Ann. Math. Statist., 33, 1065
Planck Collaboration, Ade, P. A. R., Aghanim, N., et al. 2016, A&A, 586, A138
Purcell, E. M. 1979, ApJ, 231, 404
Pilbratt, G. L., Riedinger, J. R., Passvogel, T., et al. 2010, A&A, 518, L1
Rautela, B. S., Joshi, G. C., & Pandey, J. C. 2004, BASI, 32, 159
Robitaille, T., & Bressert, E. 2012, APLpy: Astronomical Plotting Library in Python Astrophysics Source Code Library, ascl:1208.017
Rosenblatt, M. 1956, Ann. Math. Statist., 27, 832
Schaefer, B., Collett, E., Smyth, R., et al. 2007, AmJPh, 75, 163
Schmidt, G. D., Elston, R., & Lupie, O. L. 1992, AJ, 104, 1563
Serkowski, K. 1973, in IAU Symp. 52, Interstellar Dust and Related Topics, ed. J. M. Greenberg & H. C. van de Hulst (Dordrecht: Reidel), 145
Serkowski, K., Mathewson, D. S., & Ford, V. L. 1975, ApJ, 196, 261
Skrutskie, M. F., Cutri, R. M., Stiening, R., et al. 2006, AJ, 131, 1163
Sugiura, N. 1978, Comm. Statist., A7, 13
van der Walt, S., Colbert, S. C., & Varoquaux, G. 2011, CSE, 13, 22
van Leeuwen, F. 2007, A&A, 474, 653
Voshchinnikov, N. V., Das, H. K., Yakovlev, I. S., & Il'in, V. B. 2013, AstL, 39, 421
Voshchinnikov, N. V., & Hirashita, H. 2014, MNRAS, 445, 301
Wardle, J. F. C., & Kronberg, P. P. 1974, ApJ, 194, 249
Whittet, D. C. B., Gerakines, P. A., Hough, J. H., & Shenoy, S. S. 2001, ApJ, 547, 872
Whittet, D. C. B., Hough, J. H., Lazarian, A., & Hoang, T. 2008, ApJ, 674, 304
Whittet, D. C. B., Martin, P. G., Hough, J. H., et al. 1992, ApJ, 386, 562
Whittet, D. C. B., & van Breda, I. G. 1978, A&A, 66, 57
Wilking, B. A., Lebofsky, M. J., & Rieke, G. H. 1982, AJ, 87, 695
Wright, E. L., Eisenhardt, P. R. M., Mainzer, A. K., et al. 2010, AJ, 140, 1868